International Journal of Heat and Fluid Flow 31 (2010) 1–18

Contents lists available at ScienceDirect

International Journal of Heat and Fluid Flow

journal homepage: www.elsevier.com/locate/ijhff

Effect of Coriolis forces in a rotating channel with dimples and protrusions

Mohammad A. Elyyan, Danesh K. Tafti *

High Performance Computational Fluids-Thermal Sciences and Engineering Lab, Mechanical Engineering Department, Virginia Polytechnic Institute and State University, Blacksburg, VA 24061, USA

ARTICLE INFO

Article history:
Received 26 December 2008
Received in revised form 5 October 2009
Accepted 10 October 2009
Available online 5 December 2009

Keywords:
LES
Dimples
Internal cooling
Rotating channels

ABSTRACT

Large-eddy simulations are used to investigate the effect of Coriolis forces and dimple depth on heat transfer and friction in a channel with dimples and protrusions on either side. Two geometries with two different dimple–protrusion depths, $\delta = 0.2$ and 0.3 of channel height are investigated over a wide range of rotation numbers, $Ro_b = -0.77$ to 1.10 based on mean velocity and channel height. It is found that the dimple side of the channel is much more sensitive to destabilizing rotational Coriolis forces than the protrusion side of the channel, although both dimples and protrusions react to the stabilizing effects of Coriolis forces on the leading side. The dimpled surface on the trailing side experiences a large increase in heat transfer coefficient from an augmentation ratio of 1.9 for stationary flow to 3.5 at $Ro_b = 0.77$ for $\delta = 0.2$, and from 2.3 to a maximum of 3.8 for $\delta = 0.3$. Placing protrusion on the trailing side, however, only increases the augmentation ratio to between 3.25 and 3.7 from the stationary values of 3.0 and 3.4 for $\delta = 0.2$ and 0.3, respectively. The dimpled leading side experiences a large drop in heat transfer to between augmentation ratios of 1.1 and 1.4 for the two dimple depths. The protrusion surface on the leading side also experiences a large drop in augmentation from 3.0 for a stationary channel to 1.3 at $Ro_b = 0.77$ for $\delta = 0.2$ and from 3.4 to 1.8 at $Ro_b = 1.1$ for $\delta = 0.3$. The results lead to the conclusion that for low rotation numbers $|Ro_b| < 0.2$, placing protrusions on the trailing side is advantageous, whereas for $|Ro_b| > 0.2$, dimples on the trailing side of the duct give better overall performance. Between the two depths, the deeper dimple/protrusion ($\delta = 0.3$) gives higher heat transfer augmentation at the price of more frictional losses ranging from 6 to 10 versus 3 to 5 for depth $\delta = 0.2$.

© 2009 Elsevier Inc. All rights reserved.

1. Introduction

Modern gas turbine blades are exposed to increasingly higher gas temperatures which exceed the melting point of the blade material. Thus active cooling plays a critical role in maintaining the structural integrity of the blade. Blades are cooled by extracting bleed air from the compressor and passing it through internal passages inside the airfoil and then ejecting it through holes onto the blade surface to form a protective layer between the hot mainstream gases and the blade surface.

In order to enhance internal cooling, different techniques that increase the heat transfer area and promote turbulence inside the channels are applied. The most common surface enhancements used for heat transfer augmentation of internal cooling are pin fins and ribs, which produce acceptable levels of heat transfer augmentation but the pressure drop penalty can be significant. Friction ratios (C_f/C_{fo}) and Nusselt augmentation (Nu/Nu_o) of 10–20 and 2–5, respectively are common for rib turbulators and pin fins (Ligrani et al., 2003).

Flow structure inside rotating channels is quite complex under the action of the turbulence promoters and rotational Coriolis forces. The flow structure and heat transfer distribution inside rotating channels have been thoroughly investigated in the past three decades; where the rotation number, centrifugal buoyancy, and passage geometry were found to be the dominant factors affecting the heat transfer in the channel (Wagner et al., 1991a,b). Under the action of rotation, heat transfer from trailing surface increases due to flow destabilization with rotation number, and it decreases at the leading surface due to flow stabilization (Fann et al., 1994; Johnson et al., 1994; El-Husayni et al., 1994; Parson et al., 1995; Dutta and Han, 1996; Griffith et al., 2002; Al-Hadhrami and Han, 2003; Hseih and Chin, 2003; Sewall and Tafti, 2008). El-Husayni et al. (1994) and Parson et al. (1995) studied the heating condition effect on the performance of 60° and 90° ribbed square ducts, respectively. Moreover, the model orientation was reported to have an impact on the performance of the channel, where the 45° (or 135°) orientation of the channel was found to provide better performance of the channel (El-Husayni et al., 1994; Parson et al., 1995; Dutta and Han, 1996; Griffith et al., 2002; Al-Hadhrami and Han, 2003).

Murata and Mochizuki (1999) and Abdel-Wahab and Tafti (2004) studied the effect of Coriolis forces in rotating ribbed duct

* Corresponding author. Tel.: +1 540 231 9975.
E-mail address: dtafti@vt.edu (D.K. Tafti).
URL: http://www.hpcfd.me.vt.edu (D.K. Tafti).

0142-727X/$ - see front matter © 2009 Elsevier Inc. All rights reserved.
doi:10.1016/j.ijheatfluidflow.2009.10.002

Nomenclature

C_f	fanning friction coefficient
D	dimple imprint diameter
D_h	hydraulic diameter
g^{ij}	contravariant metric tensor
F	external force term
G	filter
H	channel height
k	thermal conductivity
L_x	periodic length
n	surface normal vector
Nu	surface Nusselt number
P	span-wise pitch
p	fluctuating, modified, or homogenized pressure
Pr	Prandtl number
q''	constant heat flux on channel walls
Q_x	mass flow rate in the stream-wise direction
Re	reynolds number ($=uH/\nu$)
Ro	rotation number ($=\omega_z H/u$)
S	stream-wise pitch
$\vec{u}$	cartesian velocity vector
$\vec{x}$	physical coordinates
$\vec{\xi}$	computational coordinates
δ	dimple depth
Ω	heat transfer surface area
β	mean pressure gradient
γ	mean temperature gradient
θ	fluctuating, modified or homogenized temperature
ρ	density
τ_{weq}	equivalent wall shear
ω_z	rotation speed of the channel around the z-axis

Subscripts

b	bulk
f	fluid
o	smooth channel
t	turbulent parameters
τ	values based on friction velocity

Superscripts

$*$	dimensional quantity
+	wall units
$-$	grid filtered quantity
^	test filtered quantity

using LES, where they reported the heat transfer levels to decrease and increase on the leading and trailing sides, respectively. By isolating Coriolis forces from centrifugal buoyancy effects, Abdel-Wahab and Tafti (2004) showed that Coriolis forces had a stronger effect on heat transfer from the channel than centrifugal buoyancy. They reported that centrifugal buoyancy yielded an increase of about 10% in the overall augmentation over the Coriolis forces alone, which agrees with the conclusion of Johnson et al. (1994) that centrifugal buoyancy does not have a large impact in well mixed flows.

In the present study, new surface geometries based on dimples and protrusions are proposed and investigated for internal blade cooling applications. Heat augmentation using spherical indentations (dimples) has received wide attention lately due to their good heat transfer characteristics and low pressure drop penalty (Afanasyev et al., 1993). Several researchers have investigated the effect of different geometry parameters on heat transfer characteristics of the channels, where they reported that the channel height (H/D) and dimple depth (δ/D) have the largest impact on the heat characteristics of dimpled surfaces (Moon et al., 2000; Ligrani et al., 2001a; Mahmood and Ligrani, 2002; Won et al., 2005).

The use of dimples/protrusions on opposite sides for heat augmentation in a channel was investigated by Ligrani et al., (2001b) and Mahmood et al. (2001), where they have reported higher friction and Nusselt number than the dimple/dimple case. Elyyan et al. (2008) used LES to investigate the flow structure and heat transfer distribution in a stationary channel with dimple–protrusion in the laminar to fully turbulent regime; in addition they also investigated the effect of dimple depth with respect to channel height where they reported a large impact in the low Reynolds number regime.

Despite their good heat transfer characteristics in stationary channels, the work of Griffith et al. (2003) is the only experimental study in the literature that has investigated the use of spherical indentations for cooling of rotating turbine blades. They studied the effect of rotation on heat transfer enhancement in a dimple–dimple channel with aspect ratio (AR = 4) in the Reynolds number range $Re_{Dh} = 5000–40{,}000$ and low rotation number range ($Ro_b = 0.01–0.3$), where they have reported a behavior similar to that of a ribbed channel. No detailed flow structure, heat transfer distribution, or pressure drop data was reported.

Elyyan and Tafti (2008) used LES to perform a detailed investigation of the Coriolis forces effect on flow structure and heat transfer distribution in a rotating channel with dimples on the trailing side and protrusions on the leading side. They showed the existence of secondary flow structures induced by the Coriolis forces acting on the domain and flow destabilization/stabilization near the trailing/leading surfaces, which led to about 90% increase of heat transfer near the trailing (dimple) surface and about 50% drop in heat transfer near the leading (protrusion) surface.

In this paper, we extend our analysis of the Coriolis forces effect on a rotating channel with dimples and protrusion to investigate the effect of rotation direction and dimple depth on flow structure, turbulent statistics, and heat transfer distribution on the channel surfaces. Two dimple (protrusion) depths ($\delta/H = 0.2$ and 0.3) are considered in the current study. We cover a wide range of rotation numbers from $Ro_b = -0.77$ to 1.1, at a nominal Reynolds number of 12,000. The paper describes in detail the mean and turbulent structure of the flow and the subsequent friction and heat transfer characteristic over the full range of rotation numbers.

2. Channel geometry, computational domain, and governing equations

Fig. 1 shows the channel geometry used in this study which consists of aligned dimples and protrusions on opposite surfaces. Since dimple depth was found to have a strong impact on the flow structure and heat transfer in stationary channels, we consider two dimple depths: Case 1 with $\delta = 0.2$ and Case 2 with $\delta = 0.3$. Both geometry cases have a dimple and protrusion stream-wise and span-wise pitch of $S = P = 1.62$, and dimple imprint diameter $D = 1.0$. Note that all channel dimensions are non-dimensionalized by the channel height (H^*).

The computational domain simulates two parallel plates roughened by dimples and protrusions on opposite sides and assumes fully-developed hydrodynamic and thermal flow (Fig. 1). For stationary ribbed ducts it is known that a nominally fully-developed

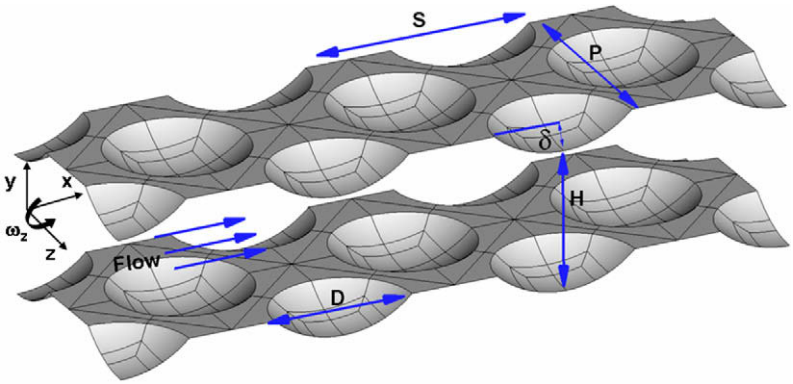

Fig. 1. Dimpled channel geometry.

flow is reached within 3–4 rib pitches from the duct entrance (Sewall, 2005). However, the developing length is much longer in a rotating duct and takes up to 8–9 rib pitches for the Coriolis driven effects to reach a spatially stationary state (Sewall, 2005). Hence the assumption of fully-developed flow and heat transfer may not exactly represent an actual cooling passage in a rotating blade. However, the assumption does not distort the physics of rotational effects and is valid in evaluating different geometries at different rotation numbers without much loss of generality in extending the conclusions to a developing flow. Using the fully-developed assumption, the channel is assumed to be periodic in the stream-wise and span-wise directions, and rotating at a uniform angular velocity (ω_z^*) orthogonal to an axis aligned with the z-axis. Channel surfaces exposed to the flow, i.e. dimple and protrusion surfaces, are heated with a constant heat flux (q''^*). The channel height (H^*),[1] friction velocity ($u_\tau^* = \sqrt{\tau_{weq}^*/\rho^*}$), and a temperature scale given by ($q''^* H^*/k^*$) are used to non-dimensionalize the governing equations of the system as will be shown later.

A special treatment of the pressure and temperature variables is required to accommodate the periodicity boundary condition of the channel (Patankar et al., 1977). In this treatment, the pressure and temperature variables are decomposed into mean and fluctuating parts as shown in the following non-dimensional equation

$$P^*(\vec{x}^*, t^*) = P_{in}^* - \beta^* x^* + p^*(\vec{x}^*, t^*) \tag{1a}$$

$$T^*(\vec{x}^*, t^*) = T_{in}^* - \gamma^* x^* + T'^*(\vec{x}^*, t^*) \tag{1b}$$

where the mean pressure and temperature gradients, β^* and γ^*, are found by performing momentum and energy balances, respectively. The non-dimensional pressure and temperature gradients are given as

$$\beta = \frac{4}{D_h} \tag{2}$$

$$\gamma = \frac{\Omega}{Re_\tau Pr Q_x L_x} \tag{3}$$

The non-dimensional[2] continuity, momentum and energy equations in transformed coordinates after incorporating the modified variables take the form

Continuity:

$$\frac{\partial}{\partial \xi_j}\left(\sqrt{g}\overline{U^j}\right) = 0 \tag{4}$$

Momentum:

$$\frac{\partial}{\partial t}(\sqrt{g}\overline{u}_i) + \frac{\partial}{\partial \xi_j}(\sqrt{g}\overline{U^j}\overline{u}_i) = \frac{\partial}{\partial \xi_j}\left(\sqrt{g}\left(\vec{a}^j\right)_i \overline{p}\right) + \frac{\partial}{\partial \xi_j}\left(\left(\frac{1}{Re_\tau} + \frac{1}{Re_t}\right)\sqrt{g}g^{jk}\frac{\partial \overline{u}_i}{\partial \xi_j}\right) + F_i \tag{5}$$

Energy:

$$\frac{\partial}{\partial t}(\sqrt{g}\overline{\theta}) + \frac{\partial}{\partial \xi_j}(\sqrt{g}\overline{U^j}\overline{\theta}) = \frac{\partial}{\partial \xi_j}\left(\left(\frac{1}{PrRe_\tau} + \frac{1}{Pr_t Re_t}\right)\sqrt{g}g^{jk}\frac{\partial \overline{\theta}}{\partial \xi_j}\right) - \sqrt{g}\gamma\overline{u}_1 \tag{6}$$

where $\vec{a}^i$ are the contravariant vectors,[3] $\sqrt{g}$ is the Jacobian of transformation, g^{ij} are the elements of the contravariant metric tensor, $\sqrt{g}U^i = \sqrt{g}(\vec{a}^j)_i u_i$ is the contravariant flux vector, $\bar{u}_i$ is the Cartesian velocity vector, Re_τ is the Reynolds number based on the friction velocity (u_τ), and θ is the modified temperature. The overbar denotes grid filtered quantities; where $\overline{G}$ is the implicit top hat filter given by

$$\overline{G}(x_i - x_i') = \begin{cases} \frac{1}{\triangle x_i}; & |x_i - x_i'| \leqslant \overline{\triangle x_i}/2 \\ 0; & \text{otherwise} \end{cases} \tag{7}$$

where $\overline{\triangle x_i}$ is the grid spacing. Re_t is the inverse of the non-dimensional turbulent eddy viscosity

$$\frac{1}{Re_t} = C_s^2(\sqrt{g})^{2/3}|\overline{S}| \tag{8}$$

where $|\overline{S}|$ is the magnitude of the strain rate tensor given $|\overline{S}| = \sqrt{2\overline{S_{ik}}\overline{S_{ik}}}$ by; and the strain rate tensor is given by

$$\overline{S_{ij}} = \frac{1}{2}\left(\frac{\partial \overline{u_i}}{\partial x_j} + \frac{\partial \overline{u_i}}{\partial x_i}\right) \tag{9}$$

and the Smagorinsky constant C_s^2 is calculated using the Dynamic subgrid stress model (Germano et al., 1991). To calculate this constant, a second filter, test filter, denoted by $\widehat{G}$ is applied to the filtered governing equations with the characteristic length of $\widehat{G}$ being larger than that of the grid filtered, $\overline{G}$. The test filtered quantity is obtained from the grid filtered quantity by a second-order trapezoidal filter which is given by $\widehat{\varnothing} = \frac{1}{4}(\overline{\varnothing}_{i-1} + 2\overline{\varnothing}_i + \overline{\varnothing}_{i+1})$ in computational coordinates in one dimension. The resolved turbulent stresses, representing the energy scales between the test and the grid filters, $L_{ij} = \widehat{\overline{u_i}\overline{u_j}} - \widehat{\overline{u}_i}\widehat{\overline{u}_j}$, are then related to the subtest, $T_{ij} = \widehat{\overline{u_i}\overline{u_j}} - \widehat{\overline{u}_i}\widehat{\overline{u}_j}$, and subgrid-scale stresses $\tau_{ij} = \overline{u_i u_j} - \overline{u_i}\,\overline{u_j}$, through the identity $L_{ij} = T_{ij} - \widehat{\tau}_{ij}$.

[1] The asterisk ($*$) is used to denote dimensional quantities.

[2] Henceforth, all usage is in terms of non-dimensional quantities unless qualified with an asterisk.

[3] The notation $(\vec{a}^j)_k$ is used to denote the kth component of vector $\vec{a}^j \cdot (\vec{a}^j)_k = \partial \xi_j / \partial x_k$.

The anisotropic subgrid and the subtest-scale stresses are then formulated in terms of the Smagorinsky eddy viscosity model as

$$\hat{\tau}_{ij} = -2C_s^2(\sqrt{g})^{2/3}\widehat{|\bar{S}|\bar{S}_{ij}}$$
$$T_{ij}^a = -2C_s^2 \propto (\sqrt{g})^{\frac{2}{3}}\widehat{|\bar{S}|\bar{S}_{ij}}$$

Using the identity

$$L_{ij}^a = L_{ij} - \frac{1}{3}\delta_{ij}L_{kk} = -2C_s^2 \propto (\sqrt{g})^{2/3}\left(\widehat{|\bar{S}|\bar{S}_{ij}} - \widehat{|\bar{S}|\bar{S}_{ij}}\right)$$
$$= -2C_s^2 \propto (\sqrt{g})^{\frac{2}{3}}M_{ij} \quad (10)$$

Here α is the square of the ratio of the characteristic length scale associated with the test filter to that of the grid filter and is taken to be $\alpha = \left[\frac{\widehat{\Delta_i}}{\overline{\Delta_i}}\right]^2 = 6$ for a three-dimensional test filtering operation (Najjar and Tafti, 1996). Using the least-square minimization procedure presented by Lilly (1992), the dynamic Smagorinsky constant can be calculated as:

$$C_s^2 = -\frac{1}{2}\left(1/(\sqrt{g})^{\frac{2}{3}}\right)\left(\frac{L_{ij}^a \cdot M_{ij}}{M_{ij} \cdot M_{ij}}\right) \quad (11)$$

where the local value of C_s^2 is constrained to positive values. The turbulent Prandtl number is assumed to have a constant value of 0.5 (Moin et al., 1991) in Eq. (6).

The Coriolis forces and mean pressure gradients effect (β) are included in the momentum equation through an external force term, F_i:

$$F_i = \sqrt{g}\beta\delta_{i1} - 2\sqrt{g}(Ro_\tau)\bar{u}_m\epsilon_{i3m} \quad (12)$$

where ϵ_{i3m} is the permutation tensor or Levi–Civita symbol. Note that the mean centrifugal buoyancy term is implicitly absorbed into the mean pressure term in the x-momentum equation. No slip and constant heat flux boundary condition are imposed at the domain walls

$$\vec{u} = 0 \quad (13)$$
$$\nabla\theta \cdot \vec{n} = 1 - \gamma\vec{e}_x \cdot \vec{n} \quad (14)$$

and periodic boundary conditions are applied at the stream-wise and span-wise edges of the domain

$$\varnothing(X_i + L_i) = \varnothing(X_i), \quad \varnothing = \vec{u}, p, \text{ and } \theta, \text{ and } i = 1 \text{ and } 3 \quad (15)$$

3. Numerical method

The non-dimensional generalized Navier–Stokes and energy equations are solved on a non-staggered grid topology, where the pressure, temperature and Cartesian velocities are solved and stored at the cell centers and the fluxes are calculated at the cell faces. Conservative finite-volume formulation with a second-order accurate central difference scheme is used to discretize the governing equations. A predictor–corrector scheme is used for time advancement of the solution, where an intermediate velocity is calculated at the predictor step which is then corrected by satisfying discrete continuity at the corrector step. Advancement in time for the energy equation is performed using the predictor step.

Simulations are performed using the computer program GenIDLEST (Generalized Incompressible Direct and Large-Eddy Simulation of Turbulence). GenIDLEST has been used to study flow structure and heat transfer in compact heat exchangers (Cui and Tafti, 2002) and in stationary and rotating ribbed ducts (Sewall et al., 2006; Viswanathan and Tafti, 2005) and has been validated extensively with experimental results. Details about the computer program and its capabilities can be found in Tafti (2001).

4. Calculation of Nusselt number and friction coefficient

Pressure drop and heat transfer of the channel are evaluated by using the friction coefficient, C_f, and Nusselt number, Nu, of the domain. The friction coefficient and Nusselt number are calculated as (the asterisk indicates dimensional quantities)

$$C_f = \frac{\tau_{weq\nu}^*}{\frac{1}{2}(\rho^* U_b^{*2})} = \frac{\beta D_h}{2U_b^2} \quad (16)$$
$$Nu = \frac{q''^* H^*}{k_f^*(T^* - T_{ref}^*)} = \frac{1}{(\theta - \theta_{ref})} \quad (17)$$

where θ_{ref} is the mean-mixed temperature of the flow defined as

$$\theta_{ref} = \frac{\int\int\int |u_x|\theta dA_x dx}{\int\int |u_x| dA_x dx} \quad (18)$$

The surface-averaged Nusselt number at the two channel walls is calculated by integrating over the surface (S)

$$Nu_{avg} = \frac{\int\int ds}{\int\int(\theta - \theta_{ref})ds} \quad (19)$$

and the overall average Nusselt number of the channel is calculated by taking the mean of the leading and trailing surface Nusselt numbers.

Nusselt number and friction coefficient of a smooth channel are used to evaluate the augmentation ratios of Nusselt number and friction coefficient. Those are obtained using the Petukhov and Gielinski correlations for C_f and Nu (Incropera and Dewitt, 2002), respectively:

$$C_{fo} = (1.580\ln(Re_H) - 2.185)^{-2}; \quad 1500 \leqslant Re_H \leqslant 2.5 \times 10^6 \quad (20)$$
$$Nu_o = \frac{(C_{fo}/2)(Re_H - 500)Pr}{1 + 12.7(C_{fo}/2)\frac{1}{2}(Pr^{2/3} - 1)}; \quad 1500 \leqslant Re_H \leqslant 2.5 \times 10^6 \quad (21)$$

Note that the original Petukhov and Gnielinski correlations are rewritten here in terms of Re_H rather than Re_{Dh}, where $Re_{Dh} = 2Re_H$ for smooth parallel plates.

5. Domain and grid independency studies

A domain independency study is conducted to obtain the smallest spatial unit capable of capturing the relevant flow structures which impact friction and heat transfer predictions. Elyyan et al. (2008) conducted a domain independency study for a stationary channel that is identical to Case 1 ($\delta = 0.2$) of the current study, where we have considered three domain sizes: Domain 1 which is the minimum available spatial unit with domain size ($1 \times P/2 \times S$), Domain 2 ($1 \times P \times S$) which is twice Domain 1 in the span-wise direction, and Domain 3 ($1 \times P/2 \times 2S$) which is twice Domain 1 in the stream-wise direction (Fig. 2). The study showed that the maximum difference in the friction ratio (C_f/C_{fo}) and Nusselt number augmentation (Nu/Nu_o) from that of Case 1 was 3.5% and 5.55%, respectively, which proved the sufficiency of Domain 1 ($1 \times P/2 \times S$) for capturing the relevant flow modes.

To further investigate the sufficiency of Domain 1 for capturing the additional flow complexity induced by Coriolis forces (rotating channel), we have conducted an additional domain independency study for the same domains considered earlier, Domains 1–3, at a nominal rotation number, $Ro_b = 0.64$, and a nominal Reynolds number, $Re_H = 11{,}000$. The domain independency test results summarized in Table 1 further confirm the sufficiency of Domain 1 ($1 \times P/2 \times S$) in capturing the relevant flow structures in the domain, where the time mean Nusselt number and friction coefficient of Domain 2 are 1.9% and 3.2% different from those of Domain 1, and those of Domain 3 have differences of 2.7% and 1.4% from those of Domain 1.

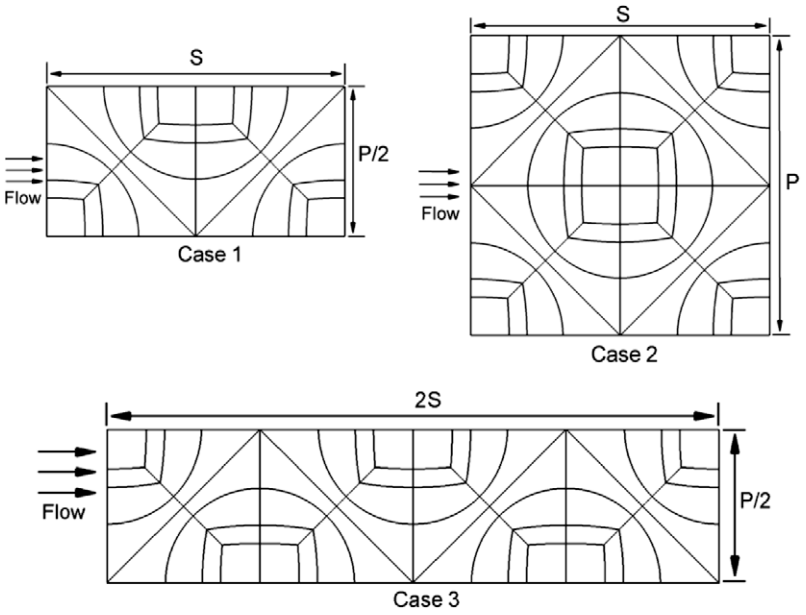

Fig. 2. Domain independency study domain Cases 1–3.

Table 1
Domain independency study for rotating channel case.

Domain case	1	2	3
Domain size	$1 \times P/2 \times S$	$1 \times P \times S$	$1 \times P/2 \times 2S$
# of cells	1,400,800	2,802,000	2,802,000
Re_H	10,900	11,100	11,000
Ro_b	0.641	0.636	0.636
Nu_{leading}	39.8	40.6	40.9
Nu_{trailing}	96.3	95.6	94.8
% Max. diff.	Ref.	1.9	2.7
C_f	0.03058	0.02961	0.03014
% Diff.	Ref.	3.2	1.4

Table 2
Grid independency results for a dimpled channel at $Re_H = 11{,}000$ rotating at $Ro_b = 0.64$.

Mesh	1	2	3	4
# of cells	466,944	933,888	1,400,832	5,603,328
Re_H	11,346	11,069	10,926	10,980
Ro_b	0.62	0.63	0.64	0.64
Nu_{leading}	39.5	40.3	39.8	38.6
Nu_{trailing}	102.5	98.1	96.3	93.7
% Max. diff.	9.4	4.7	3.0	Ref.
C_f	0.02836	0.02979	0.03058	0.03027
% Diff.	6.3	1.6	1.0	Ref.

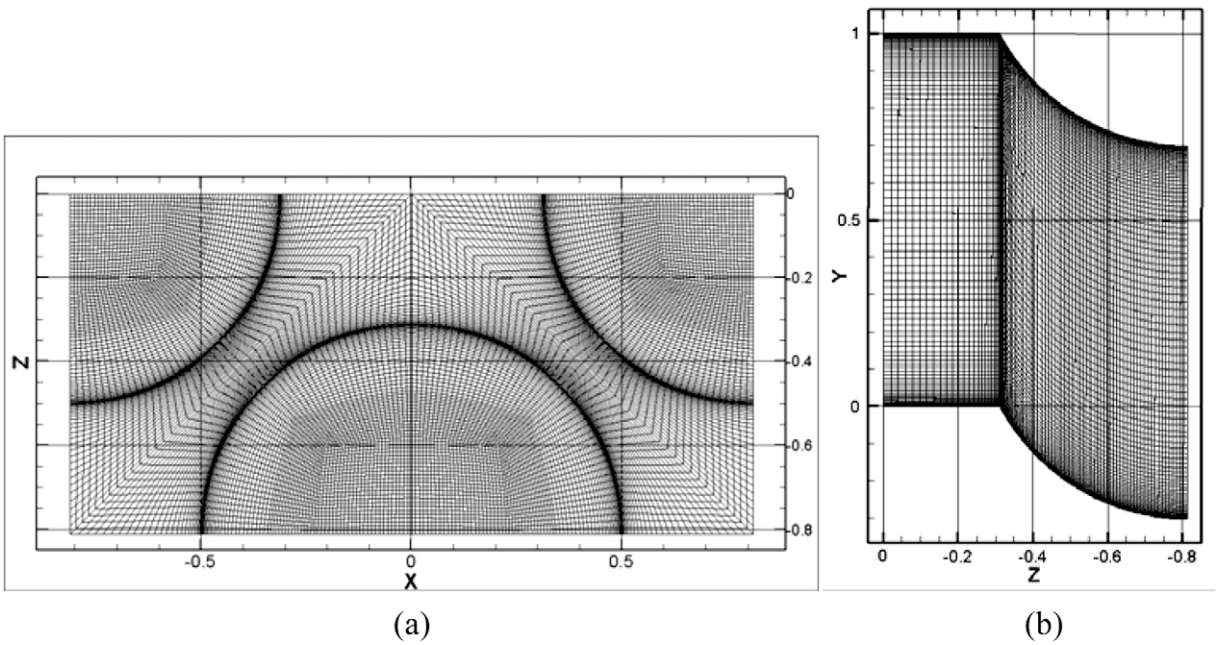

Fig. 3. (a) Surface mesh on dimpled side of channel. (b) Cross-sectional mesh. Very fine meshes are placed in the vicinity of the surfaces and at the rims of the dimple and protrusion.

Once a computational domain size was selected (Domain 1), we have performed a grid independency study using four mesh resolutions: Mesh 1 is the coarsest grid with 466,944 cells, Mesh 2 is finer than Mesh 1 in the cross-stream direction with total number of cells of 933,888, Mesh 3 is three times finer than Mesh 1 in the cross-stream direction with 1,400,832 cells, and Mesh 4 is three times Mesh 1 in the cross-stream direction and twice as fine in the wall parallel directions with a total of 5,603,328 cells. All cases are constructed using 28 grid blocks with finer mesh resolution placed in the vicinity of solid surfaces of the channel and the first grid point in the cross-stream direction was placed at an average distance of $\Delta y = 4.0 \times 10^{-4}$ from the walls for all the mesh resolutions. Calculations are performed at a nominal Reynolds number, $Re_H = 11{,}000$, and rotation number, $Ro_b = 0.64$. Table 2 summarizes the results of the grid independency test, where the finest mesh case (Mesh 4) is taken as a reference for comparison. While the

Table 3
Rotating channel cases conducted for Case 1 ($\delta = 0.2$).

Case	CW4	CW3	CW2	CW1	Stat	CCW1	CCW2	CCW3	CCW4
Ro_b	−0.70	−0.58	−0.35	−0.14	0.0	0.15	0.39	0.64	0.77
Ro_τ	−4.5	−3.5	−2.0	−0.75	0.0	0.75	2.0	3.5	4.5
Re_H	12,900	12,100	11,300	9700	9850	10,200	10,200	10,900	11,700
Re_τ	2000	2000	2000	2000	2000	2000	2000	2000	2000

Table 4
Rotating channel cases conducted for Case 2 ($\delta = 0.3$).

Case	CW3	CW2	CW1	Stat	CCW1	CCW2	CCW3	CCW4	CCW5
Ro_b	−0.75	−0.47	−0.19	0.0	0.20	0.34	0.57	0.89	1.10
Ro_τ	−3.5	−2.0	−0.75	0.0	0.75	1.25	2.0	3.5	4.5
Re_H	14,000	12,890	12,090	11,590	11,500	11,100	10,590	11,790	12,370
Re_τ	3000	3000	3000	3000	3000	3000	3000	3000	3000

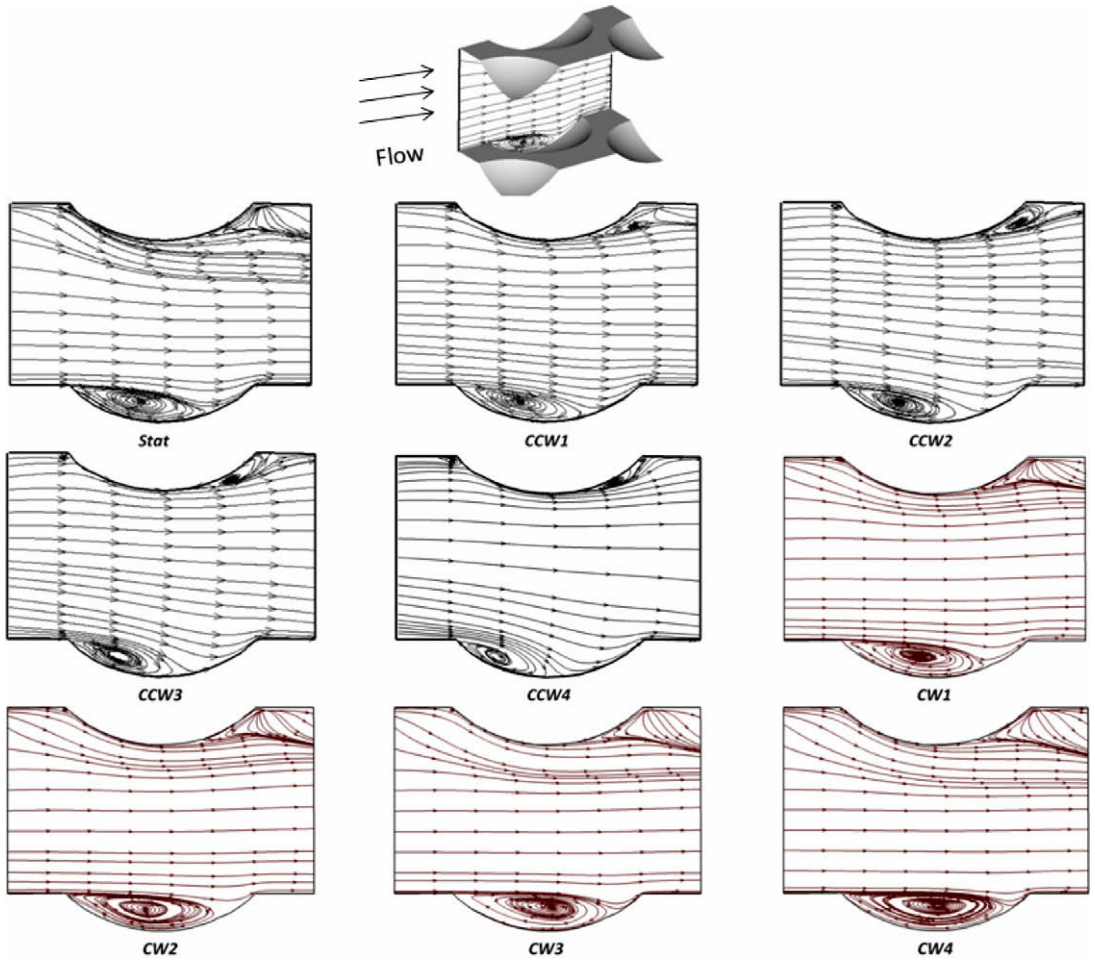

Fig. 4. Velocity streamlines at a stream-wise plane ($z = -0.81$) located at the center of the dimple/protrusion at different rotation numbers (x-velocity contours) for the stationary and rotating cases for dimple depth, $\delta = 0.2$.

error on the coarsest mesh is 9% and 6% in time mean Nusselt number and friction coefficient, these reduce to 3% and 1% on Mesh 3. Due to the relatively small gain in accuracy but at a much larger cost between Mesh 3 and 4, Mesh 3 is selected for performing the calculations in the current study with a domain size $1 \times P/2 \times S$.

Fig. 3 shows the surface and cross-sectional distribution of Mesh 3 for Case 2 ($\delta = 0.3$). Fine grid resolution is placed in the cross-stream direction in the vicinity of the solid walls of the channel with the first grid point placed at an average distance of $\Delta y = 4.0 \times 10^{-4}$ from the walls. An *a posteriori* calculation of the local friction velocity showed the average distance of the first grid point at $y_1^+ = 0.12 - 0.13$, and the surface averaged values of the wall parallel distribution as $\triangle_{//}^+$ 7–8 at the highest rotation numbers simulated.

6. Results and discussion

Tables 3 and 4 summarize the calculations conducted for Case 1 ($\delta = 0.2$) and Case 2 ($\delta = 0.3$). The friction Reynolds number Re_τ is held constant ($Re_\tau = 2000$ for $\delta = 0.2$ and $Re_\tau = 3000$ for $\delta = 0.3$), whereas the rotation number Ro_τ is varied from -4.5 to $+4.5$. Based on the balance between friction losses and the applied mean pressure gradient β, a bulk mean flow velocity is obtained from the calculation. The calculated mean velocity is then used to define Re_H and Ro_b for each calculation, which range between $10{,}000 \leqslant Re_H \leqslant 14{,}000$ and $-0.80 \leqslant Ro_b \leqslant 1.10$. During positive or counter-clockwise (CCW) rotation, the dimpled surface of the channel is on the trailing side, whereas during clockwise (CW) rotation, the protrusion side is on the trailing side of the duct. To maintain uniformity in the interpretation of data, all results are non-dimensionalized by the calculated mean bulk velocity in the channel (u_b). Nusselt numbers and friction coefficients are normalized by the baseline values given by Eqs. (11) and (12) at their respective Re_H. While the absolute values of friction coefficient and Nusselt numbers are sensitive to the Reynolds number, the augmentation ratios have negligible sensitivity to the Reynolds number variations in the range between $10{,}000 \leqslant Re_H \leqslant 14{,}000$ (Elyyan et al., 2008; Moon et al., 2000).

Each calculation is initiated with an initial best guess of velocity and temperature fields and allowed to develop under the influence of the prescribed pressure gradient. When the flow shows a statistically stationary state, temporal averaging is conducted for a typical sampling time between 5 and 10 non-dimensional time units.

6.1. Mean flow structure

The relationship between flow structure and surface heat transfer in a stationary channel with dimples and protrusions has been investigated in detail by Elyyan et al. (2008). It was established that heat augmentation on the dimpled surface was chiefly brought about by separation induced vortex impingement in the reattachment region of the dimple cavity. The ejection and redirection of these vortices and additional vortex shedding at the rim of the dimple was responsible for the high heat transfer augmentation on the flat landing downstream of the dimple. On the other

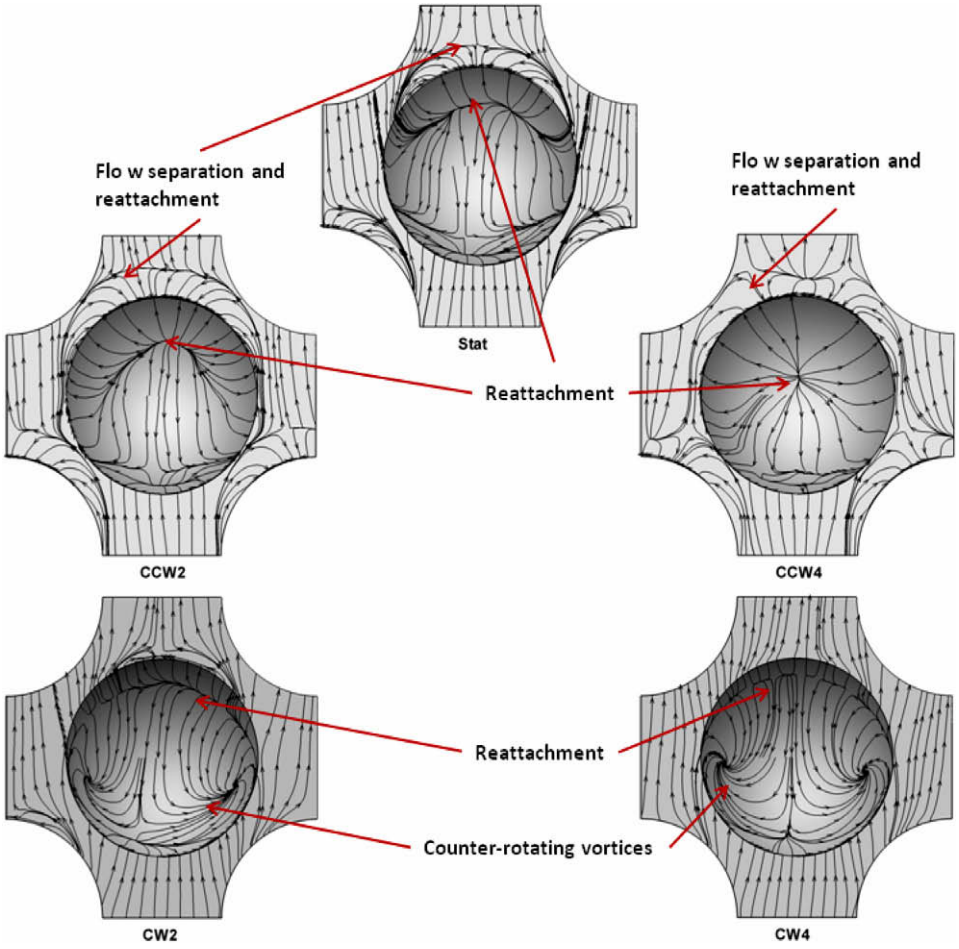

Fig. 5. Velocity friction lines near the dimple surface for Stat, CCW2, CCW4, CW2, and CW4 cases. Note that the dimple surface is the leading side for Cases CW2 and CW4, and it is the trailing side for Cases CCW2 and CCW4. Dimple depth, $\delta = 0.2$.

hand, on the protrusion side, flow impingement on protrusions and acceleration between protrusions played an important role in augmenting heat transfer. Wake turbulence also plays a role in augmenting heat transfer on the flat landing downstream of the protrusion.

Coriolis forces modify momentum transfer by adding force terms into the momentum equations. For orthogonal rotation about the z-axis, additional terms $2Ro_b v$ and $-2Ro_b u$ act as additional force terms in x- and y-momentum transfer, respectively. For positive or CCW rotation, the first-order effect is an additional net downward force in the y-momentum equation which tends to push the fluid towards the trailing wall of the channel increasing the flow rate in the bottom half. This first-order effect gives rise to secondary flow cells within the channel cross-section. The secondary flow increases in magnitude with rotation number and at high rotation numbers is found to counter the first-order effect of Coriolis forces by transporting fluid from the trailing to the leading side of the duct. An additional effect is the impact of Coriolis forces on turbulence production. Although Coriolis forces do not make a direct contribution to the production of turbulent kinetic energy, they do affect its magnitude indirectly through their action on normal stress components and the primary shear stress $\overline{u'v'}$. In turbulent channel flow, through phenomenological reasoning it can be shown that on the trailing side of the channel, terms attributed to Coriolis forces reinforce third quadrant $\overline{u'v'} < 0$ turbulence generation mechanisms of bursts and sweeps while having an opposite effect on the leading side. These are often referred to as the "destabilizing" and "stabilizing" effects of Coriolis forces. Whereas the phenomenological effects of Coriolis forces do not change from one geometry to another, its non-linear interactions with the base stationary flow and resulting impact on heat transfer augmentation through flow field modification is different from one geometry to another.

The effect of rotation on the mean flow is characterized in Figs. 4–6. Fig. 4 shows the velocity streamlines at a stream-wise plane along the dimple/protrusion centerline at $z = -0.81$ (see Fig. 3) for the stationary and rotating cases for Case 1 with dimple depth, $\delta = 0.2$. Figs. 5 and 6 plot the friction lines (or streamlines very close to the surface) on the dimple and protrusion sides of the channel, respectively to give an additional perspective on the mean flow. In a stationary duct, flow approaching the protrusion impinges and accelerates around it producing high wall shear at the sides and at the end wall between protrusions (Elyyan et al., 2008). The shear layer on the protrusion separates as it encounters an adverse pressure gradient to form a turbulent wake region behind the protrusion, which reattaches on the flat landing downstream of the protrusion. A small mean recirculating eddy is also present at the windward junction of the protrusion with the channel wall. Flow on the dimple side of the channel is characterized by turbulent shear layer separation at the windward (leading) rim of the dimple with reattachment in the dimple cavity. As the flow from the dimple cavity is ejected out along the leeward (trailing) rim of the dimple, it separates once again and reattaches on the flat landing.

The action of Coriolis forces has the following mean effect on the flow field:

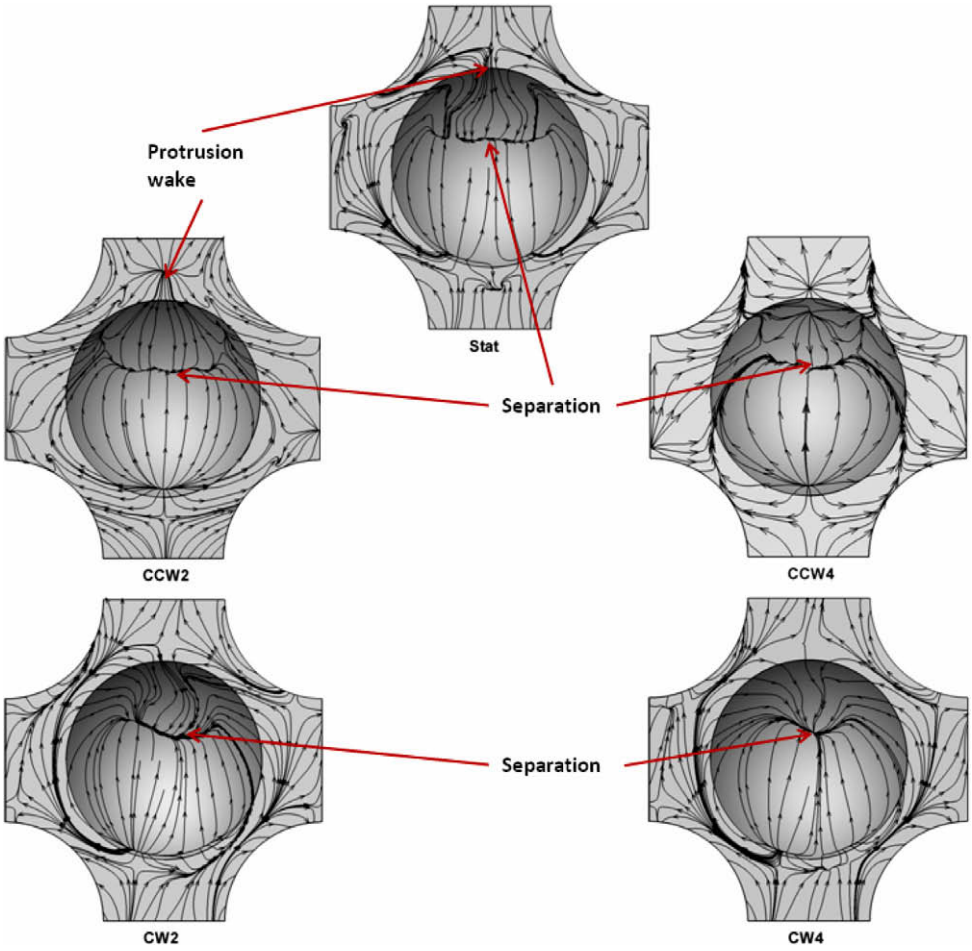

Fig. 6. Velocity friction lines near the protrusion surface for Stat, CCW2, CCW4, CW2, and CW4 cases. Note that the protrusion surface is the trailing side for Cases CW2 and CW4, and it is the leading side for Cases CCW2 and CCW4. Dimple depth, $\delta = 0.2$.

– As the channel is rotated in the counter-clockwise (CCW) direction, the dimpled side is oriented as the trailing edge with the protrusions on the leading side of the channel. The action of Coriolis forces leads to a more energetic flow on the trailing side of the channel which results in the progressive shrinking of the recirculation zone in the dimple cavity as the turbulent separated shear layer reattaches faster. The structure of the recirculation region in the dimple cavity changes from covering most of the lateral radius of the dimple to an elongated structure mostly concentrated in the center of the dimple cavity. Further, by early and more energetic reattachment in the dimple cavity, the flow ejection at the leeward rim of the dimple cavity is strengthened. Conversely, on the protrusion side of the channel, Coriolis forces make the flow less energetic resulting in a gradual growth of the wake region as the rotation number increases. Close inspection of Figs. 4 and 5 reveals that there is an increase in the extent of the wake region up to CCW2 ($Ro_b = 0.39$) after which the wake shrinks in size.
– For clockwise (CW) rotation, the flow shifts towards the protrusion side of the channel which acts as the trailing edge. The action of Coriolis forces is not as strongly evident on the flow structure as it is at the dimpled surface for counter-clockwise rotation (CCW). There is some effect on the extent of the protrusion wake which shrinks in size initially ($Ro_b = -0.35$, CW2 in Fig. 6), but which does not change significantly as rotation increases to $Ro_b = -0.70$ (CW4 in Fig. 6). An additional visible modification to the flow field is the disappearance of the junction eddy in front of the protrusion. On the leading dimpled surface, the effects of rotation are much more evident. The attenuation of turbulence leads to a less energetic flow which results in delayed reattachment of the separated shear layer in the dimple cavity and the recirculation zone extends across the whole dimple at $Ro_b = -0.70$ (CW4 in Fig. 4). There is also a noticeable weakening of the flow ejection out of the dimple cavity (CW2 and CW4 in Fig. 5) indicated by the absence of separation and reattachment around the leeward rim of the dimple. Rotation also changes the structure of the recirculating region in the dimple cavity. As the rotation number increases, two counter-rotating vortex structures become prominent inside the cavity (CW2 and CW4 in Fig. 5) and the structure of the flow in the dimple cavity approaches that observed in stationary flows at lower Reynolds numbers (Ligrani et al., 2001a; Elyyan et al., 2008).

In order to indentify the secondary flow structures induced by the Coriolis forces, mean cross-sectional streamlines 0.2D downstream of the dimple/protrusion are examined in Fig. 7. For counter-clockwise (CCW) rotation, two counter-rotating flow structures appear in the span-wise plane, one over the dimple and the other above the flat landing downstream of the dimple. The smaller structure at the rim of the dimple is a manifestation of the early flow reattachment in the cavity and the more energetic flow ejec-

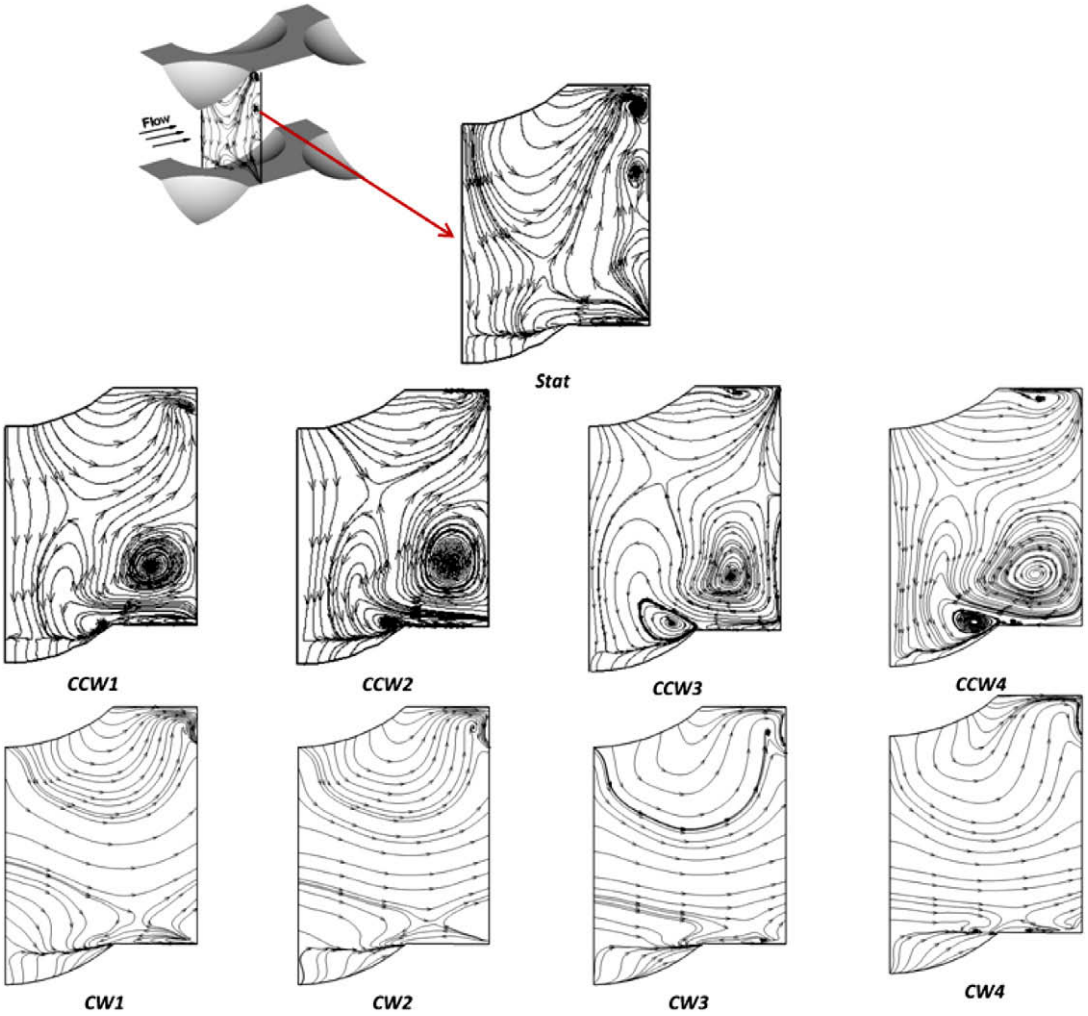

Fig. 7. Secondary flow structure at a span-wise plane located 0.2D downstream of dimple for stationary and rotating cases for $\delta = 0.2$.

tion at the rim of the dimple which imparts a rotational component to the shear layer. Whereas the larger structures which are present above the dimple and the flat landing extend from the trailing wall to midway through the channel can be attributed to Coriolis induced secondary flow. These secondary flow structures gain definition and magnitude with increasing rotation number. To provide better definition to the secondary flow structures, Fig. 8 shows selected planes covering the dimple-to-dimple stream-wise pitch at CCW4 ($Ro_b = 0.77$), which shows well-defined secondary flow cells in the cross-section over the full stream-wise pitch. It is noted that the flow cells are clearly biased towards the dimple side of the channel. On the other hand, observing Fig. 7 for clockwise rotation (CW) rotation shows no major change in the flow structure in the channel cross-section. Examination of different stream-wise planes at CW4 reveals differences with similar planes in the stationary channel, but does not reveal any differentiating organized secondary flow cells which can be clearly attributed solely to rotational effects.

Whereas streamlines give a structural view of the cross-stream flow, to obtain some quantitative measure of the secondary flow and its effect on the bulk flow, Fig. 9 shows the stream-wise (u) and cross-stream (v) velocities normalized by the bulk velocity for the CCW and CW cases at the centerline just downstream of the dimple and protrusion. It is observed that at low rotation numbers $|Ro_b| < 0.2$, the first-order effect of Coriolis forces to push the bulk flow towards the trailing wall is evident for both CCW (dimple side) and CW (protrusion side). However, in both cases (CCW and CW) as the rotation number increases above 0.2, the trend in the u-velocity profiles is reversed as the bulk flow shifts towards the leading side of the channel. This is attributed to the stronger Coriolis induced secondary flows set-up in the cross-section – as can be deduced from the cross-stream velocities in Fig. 9b, which increase with rotation number.

6.2. Turbulent kinetic energy

Turbulent kinetic energy (TKE) levels are of special interest, since they are closely connected to the rate of heat transfer from surfaces. Fig. 10 shows the TKE distribution, normalized by the bulk velocity squared, at a span-wise plane 0.2D downstream of the dimple/protrusion at different rotation numbers. For the stationary channel, high TKE levels exist in the separated shear layer inside the dimple cavity (labeled A), the turbulent wake region downstream of the protrusion (labeled B), and region C, which is the carry-over of wake turbulence from the upstream protrusion. With rotation in the positive or counter-clockwise direction (CCW), the TKE contours show: (i) concentrated high TKE levels in the separated shear layer inside the dimple cavity (labeled A); (ii) diminishing TKE levels in the wake of the protrusion (labeled B) and in region C due to the slower flow movement near the leading (protrusion) surface; (iii) higher TKE levels in the flow ejection zone at the lateral rim of the dimple cavity, which coincides with the location of the secondary flow structure identified in Figs. 7 and 8 at the same location. Note that the high TKE levels in region A that represent the separated shear layer inside the dimple cavity move closer to the dimple surface as the rotation number increases (CCW1–CCW4), which corroborates with the early reattachment observed in Fig. 4. Moreover, the TKE levels for CCW3 ($Ro_b = 0.64$) and CCW4 ($Ro_b = 0.77$) are lower than those at the lower rotation numbers. This is due to the action of the Coriolis induced secondary structures which drives the flow away from the dimple surface and corroborates with the observation made for the stream-wise velocity profile for the CCW cases, in Fig. 9.

With the protrusion on the trailing side (CW cases), the TKE contours show: (i) lower TKE levels that diminish with increasing rotation number in the separated shear layer inside the dimple cavity (region A); (ii) a smaller concentrated TKE zone in the wake

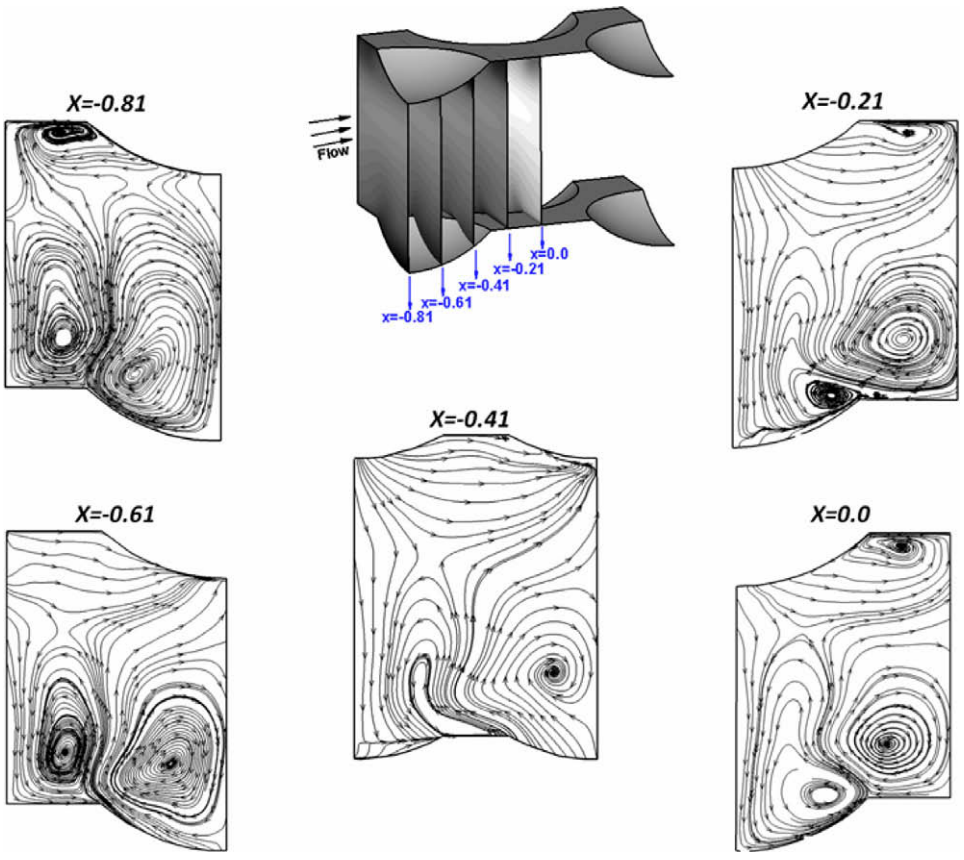

Fig. 8. Secondary flow structure at selected span-wise planes for CCW4 case for $\delta = 0.2$.

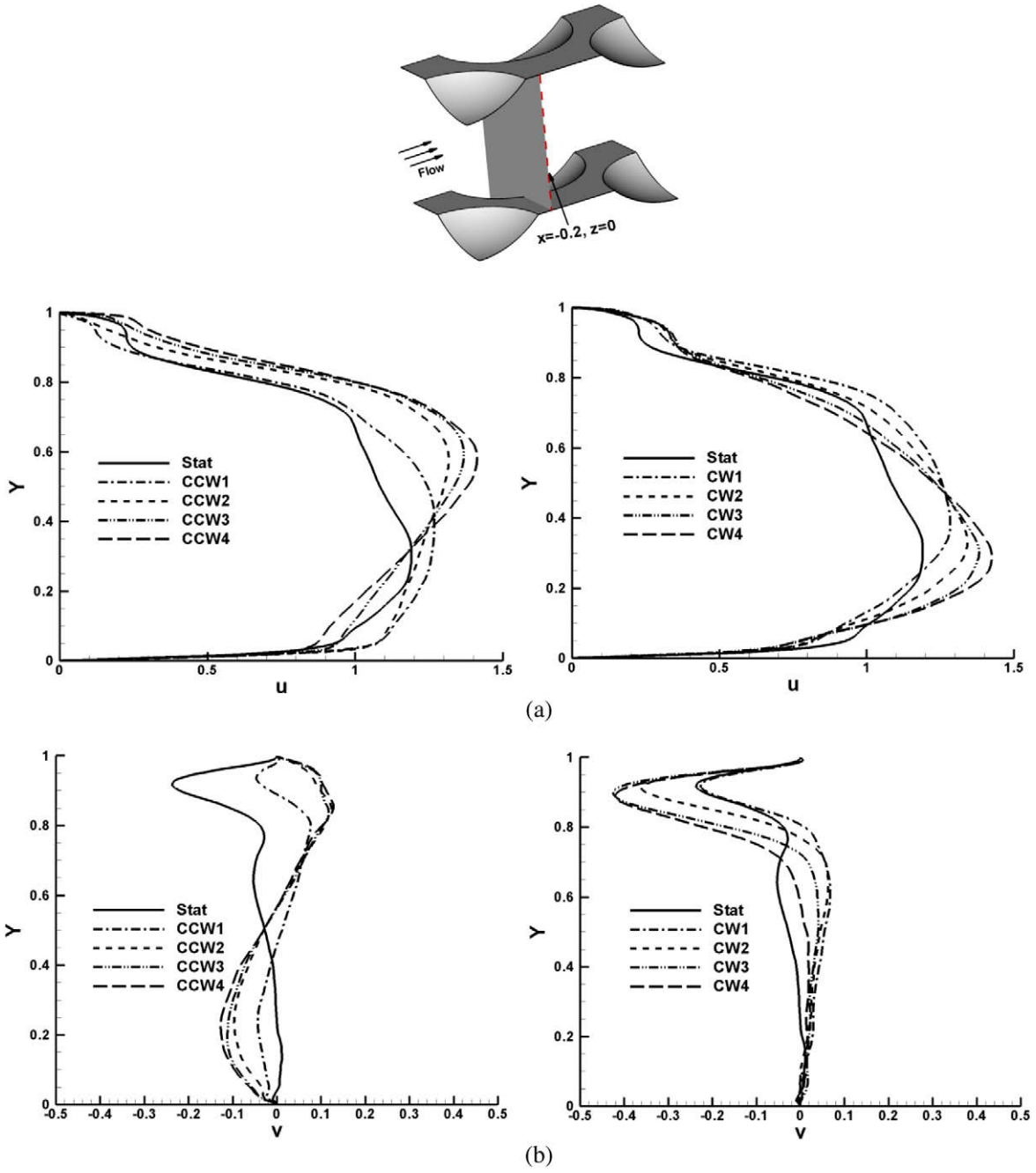

Fig. 9. Stream-wise and cross-stream velocity profiles (normalized by mean bulk velocity) for different rotation numbers at 0.2D downstream of dimple (protrusion) ($x = -0.21$) and at centerline between dimples ($z = 0.0$) for $\delta = 0.2$.

of the protrusion (B) and a magnification of region (C); and (iii) attenuation of TKE inside the dimple cavity. Note that, similar to the CCW cases, the TKE levels become weaker as the rotation number increases to $Ro_b = -0.58$ (CW3) and -0.77 (CW4) especially in the wake of the protrusion. This observation corroborates with the mean velocity profiles in Fig. 9, which indicate that as rotation number increases, flow is pushed away from the trailing towards the leading side of the channel.

Fig. 11 shows the TKE profiles at the centerline of the dimple ($z = 0$) at a plane 0.2D downstream of the dimple/protrusion ($x = -0.2$) for the CCW and CW cases. Two main peaks appear in the TKE profile. Near the dimple wall, the peak in TKE is representative of the turbulent characteristics of flow ejecting out of the dimple cavity which after separation at the rim of the dimple, reattaches in this region, and the peak at the protrusion side representing the turbulent wake of the protrusion. As the channel rotates in the CW direction (protrusion on trailing side), the maximum value of TKE increases in the wake of the protrusion at $Ro_b = -0.15$ (CW1), but starts decreasing thereafter on further increase in the rotation number. The leading side of the channel (dimples) experience a monotonic decrease in the peak value near the surface as the flow stabilizes. For counter-clockwise (CCW) rotation the opposite effects come into play. There is a steady decrease in TKE in the turbulent wake of the protrusion, while on the dimple side, the peak TKE increases initially for CCW1 but then decreases as the rotation number increases further.

Fig. 12 shows the volume-averaged TKE values for the two dimple/protrusion depths of 0.2 and 0.3. Since the heat transfer rate is

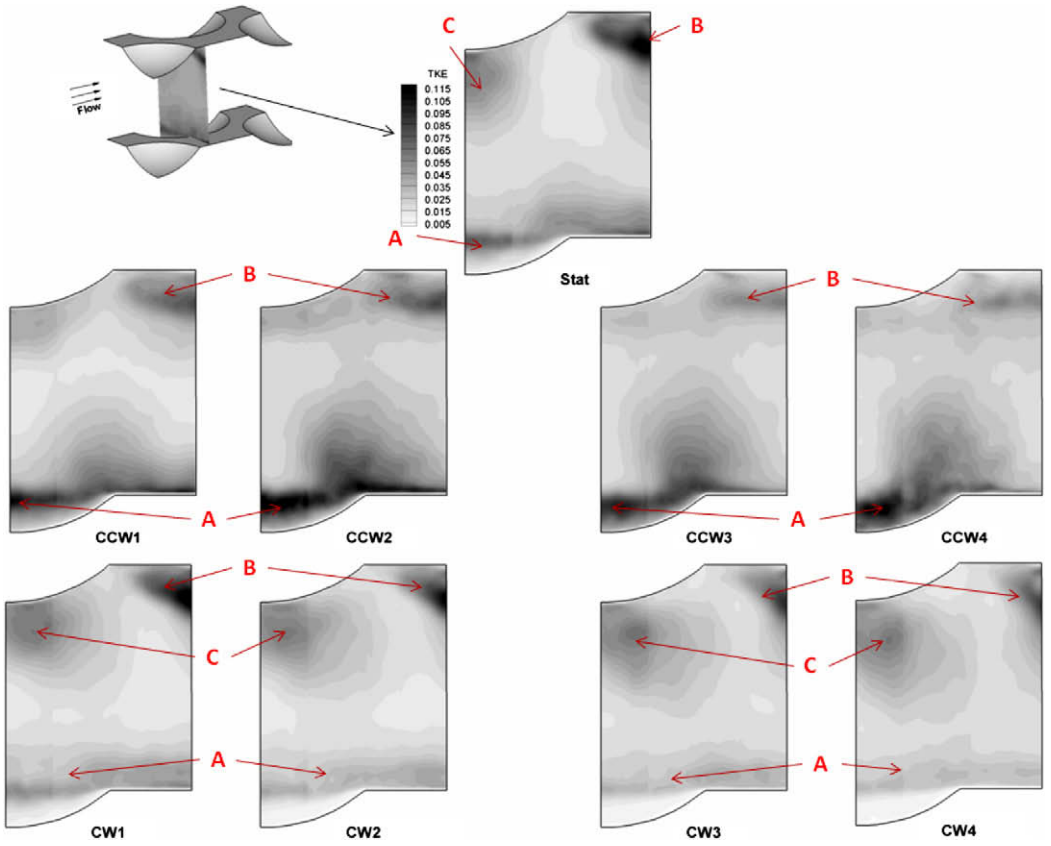

Fig. 10. Normalized T.K.E. distribution at a span-wise plane 0.2D downstream of dimple (protrusion) ($x = -0.2$) for all rotation numbers for $\delta = 0.2$.

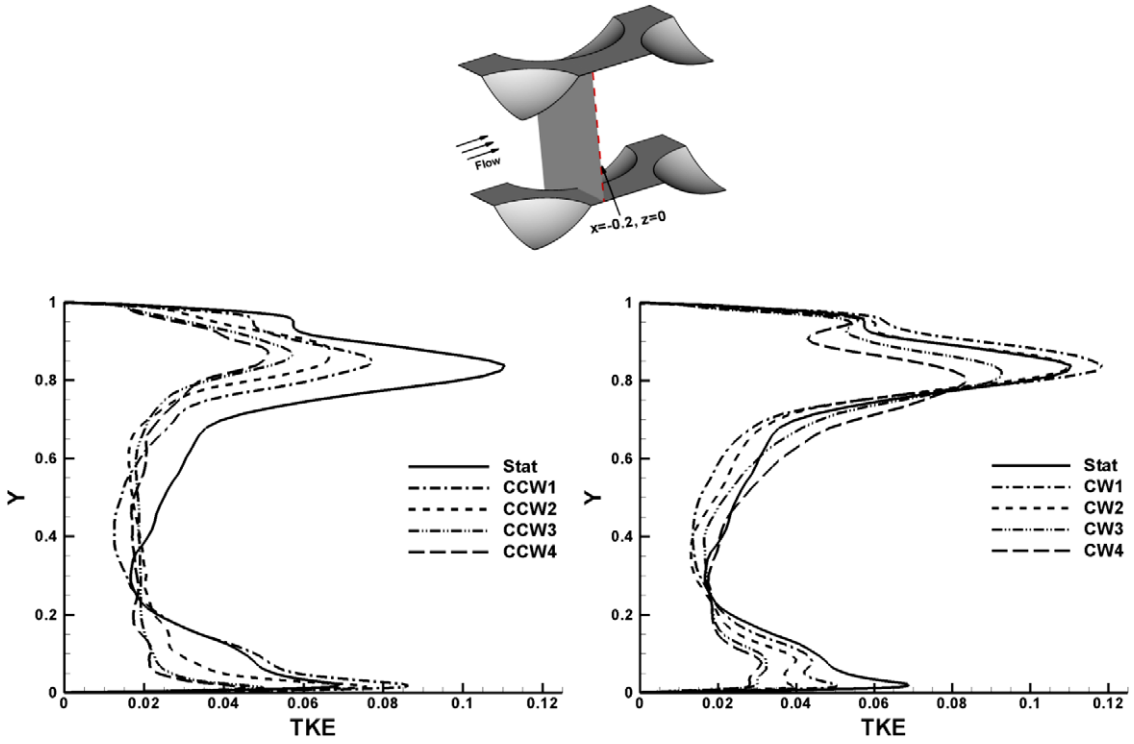

Fig. 11. TKE profile at stream-wise plane $x = -0.21$ along the centerline of the dimple/protrusion ($z = 0$) for $\delta = 0.2$.

strongly dependent on the TKE, volume-averaged TKE provides a concise indicator of heat transfer behavior. As we would expect, the deeper dimple depth geometry ($\delta = 0.3$) results in higher TKE values than the shallower dimple depth ($\delta = 0.2$). What is quite revealing though, are the predicted trends of TKE. For CCW rotation when dimples are on the trailing wall, the TKE increases up to

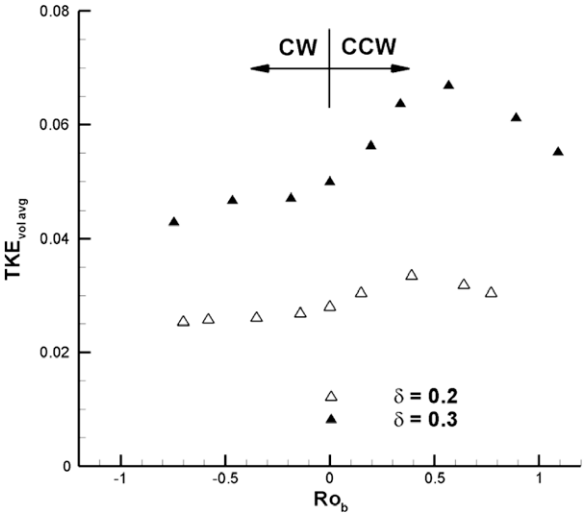

Fig. 12. Volume averaged TKE values normalized by the bulk velocity squared for all rotation cases.

about $Ro_b = 0.6$ for $\delta = 0.3$ and $Ro_b = 0.5$ for $\delta = 0.2$, after which it decreases as rotation number increases further. On the other hand, for CW rotation the volume-averaged TKE decreases with rotation number. This trend implies that CCW rotation is much more successful in augmenting turbulence on the dimpled surface (trailing side) than it is on the protrusion side of the channel during CW rotation. It will be shown later that the averaged heat transfer coefficients closely mimic the trends in volume-averaged TKE.

6.3. Heat transfer distribution

Figs. 13 and 14 show contours of the time averaged Nusselt number augmentation ratio on the protrusion surface for CCW and CW rotation, respectively. In the stationary channel, regions of high heat transfer exist on the windward side of the protrusion due to flow impingement and acceleration and on the flat wall in the passage between protrusions. Low-heat transfer regions exist near the location of separation and in the wake region. The presence of the junction eddy at the windward edge of the protrusion also decreases the heat transfer (Fig. 4). With CCW rotation there is a gradual decrease in the heat transfer distribution as the flow slows down and stabilizes near the leading-protrusion surface (Fig. 13). The region of maximum heat transfer on the protrusions moves from the side of the protrusion to the center and decreases in magnitude as Ro_b increases. Similar decreases are observed on the wall in the passages between protrusions and in the wake of the protrusion.

With clockwise rotation when the protrusion surface is on the trailing side more pronounced heat augmentation is observed on the front of the protrusion (stronger flow impingement and acceleration), in the passage between protrusions and at flow reattachment downstream of the protrusion (Fig. 14). Note that these zones of high heat transfer shrink in size for the highest rotation, which is in agreement with the TKE contours and profiles seen earlier in Figs. 10 and 11. Moreover, the low-heat transfer region at flow separation at the back of the protrusion become smaller as the rotation number increases, which is due to the smaller wake and earlier flow reattachment discussed in Fig. 4.

Figs. 15 and 16 show contours of the time averaged Nusselt number ratio on the dimple surface for the CCW (trailing) and

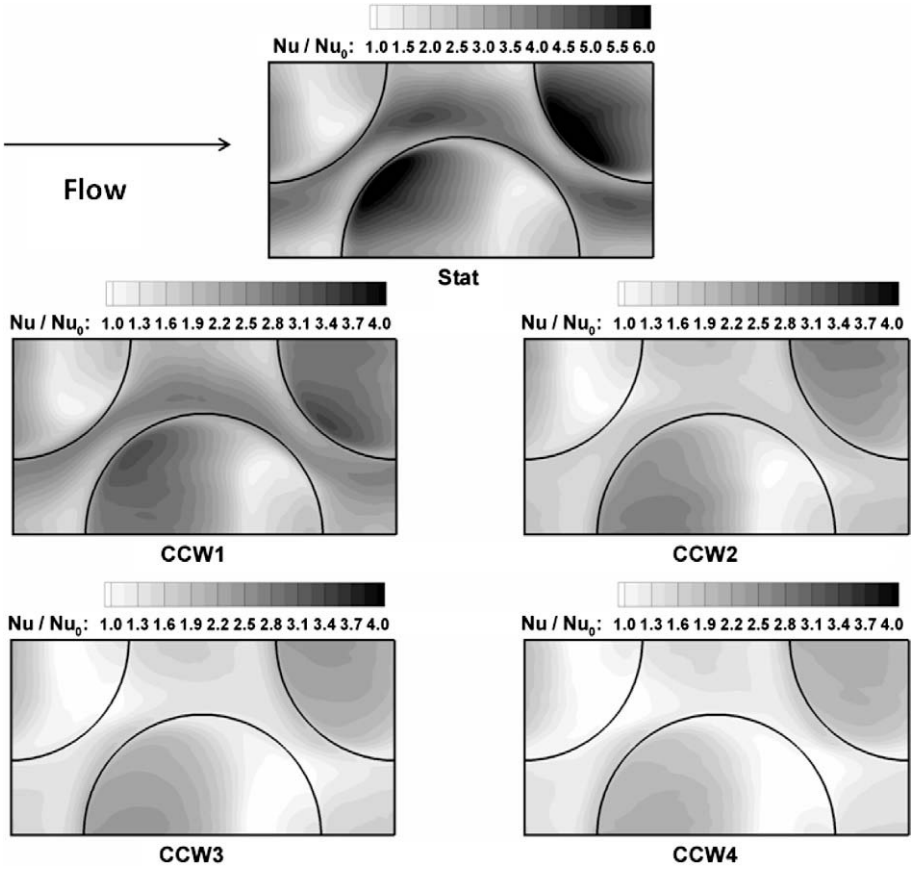

Fig. 13. Mean Nusselt number augmentation distribution on the protrusion (leading) surface for the CCW rotating channel cases (flow from left to right).

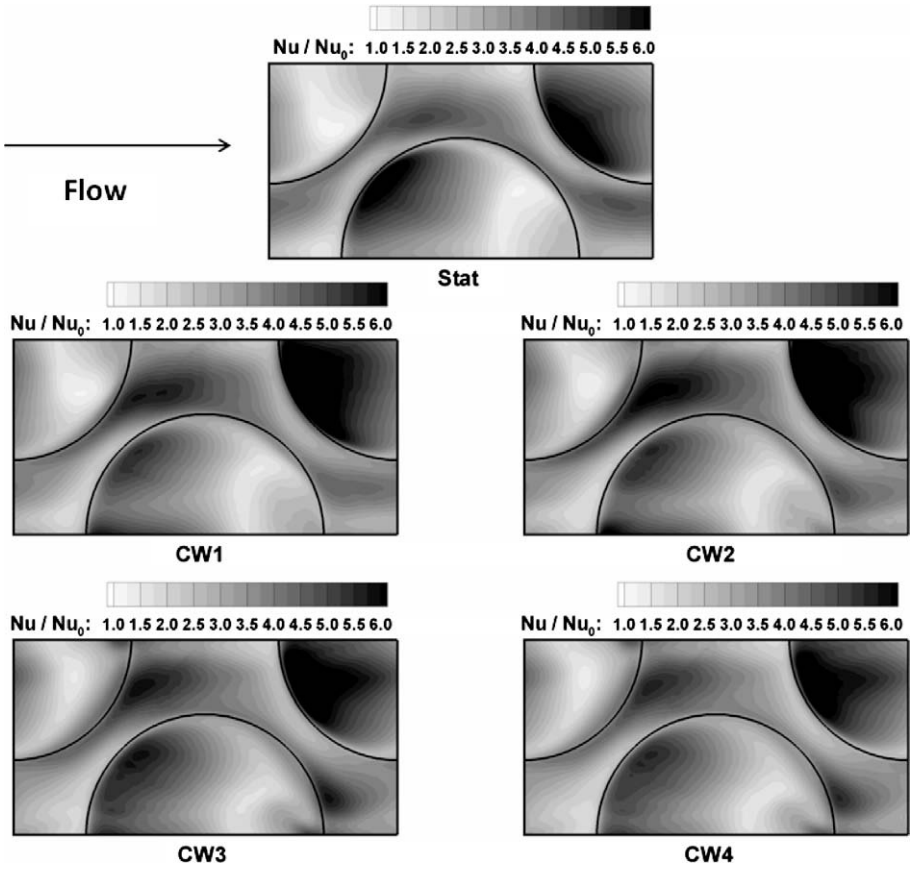

Fig. 14. Mean Nusselt number augmentation distribution on the protrusion (trailing) surface for the CW rotating channel cases (flow from left to right).

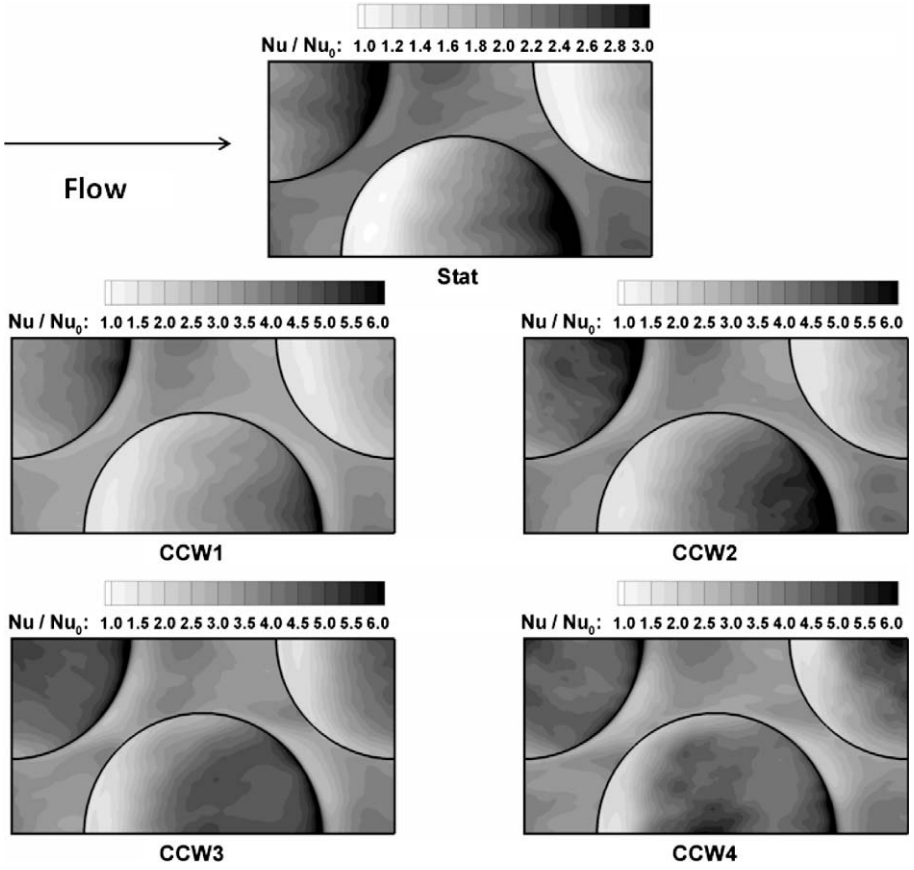

Fig. 15. Mean Nusselt number augmentation distribution on the dimple surface for the CCW rotating channel cases (flow from left to right).

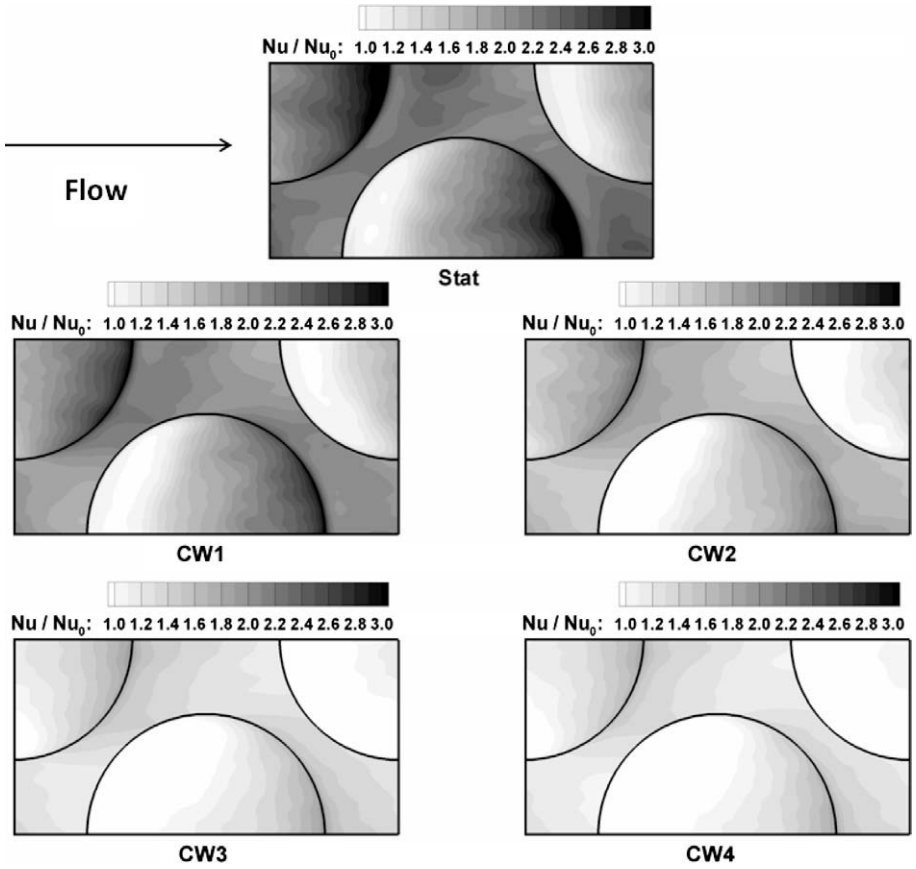

Fig. 16. Mean Nusselt number augmentation distribution on the dimple surface for the CW rotating channel cases (flow from left to right).

CW (leading) rotation, respectively. In the stationary channel, high heat transfer regions are mostly observed in the dimple cavity in the region of shear layer reattachment and acceleration of the flow as it ejects out of the dimple cavity at the leeward rim. This is followed by a region of low-heat transfer immediately downstream of the rim periphery which is caused by shear layer separation of the ejected flow followed by a region of high heat transfer when the shear layer reattaches back on the flat landing and is consistent with observations made in Fig 5. The region of flow recirculation in the upstream half of the dimple incurs the largest heat transfer penalty. On CCW rotation, the most visible effect is the higher heat transfer in the dimple cavity as the recirculation zone shrinks in size as seen earlier in Fig. 4. A counter-effect is the increase in the low-heat transfer region surrounding the leeward rim of the dimple as the rotation number increases, which is consistent with the observation of reducing TKE near the surface on the flat landing in Figs. 10 and 11. When the dimples are placed on the leading side in CW rotation (Fig. 16), there is a steady decrease in heat transfer augmentation ratio as the rotation number increases. The attenuation in heat transfer is evident over the whole leading surface especially in the dimple as the recirculation region grows to cover the full extent of the dimple cavity (Figs. 4 and 5).

6.4. Average friction coefficient and Nusselt number

Fig. 17 shows the surface-averaged Nusselt number variation with Ro_b for the two dimple–protrusion depths considered, i.e. $\delta = 0.2$ and 0.3, on the leading and trailing surfaces. The general trends for $\delta = 0.3$ follow that of $\delta = 0.2$ with some differences which will be highlighted. When the dimple surface is on the trailing side for CCW rotation, there is a sharp increase in the average Nusselt number as the channel starts rotating at $Ro_b < 0.2$ when the augmentation ratio increases from 1.8 to 2.96 for $\delta = 0.2$ and from 2.3 to 2.9 for $\delta = 0.3$. After this point, on a further increase in rotation number to $Ro_b = 0.39$, the shallower dimples with $\delta = 0.2$ increase to 3.4 and increase gradually thereafter to values in the range of 3.5 at $Ro_b = 0.64$ and 0.77. On the other hand, the deeper dimples exhibit a sharp increase in the augmentation ratio to 3.8 as the rotation number increases from $Ro_b = 0.19$ to 0.57, and decreases thereafter to values close to 3.65 as the rotation number Ro_b increases further to 0.9 and 1.1. When the dimple surface is on the leading side of the channel (CW rotation), there is a steady drop in the average augmentation ratio for both dimple depths. The augmentation ratio decreases from the stationary values of 1.8 and 2.3 to 1.1 and 1.4, for $\delta = 0.2$ and 0.3, respectively at the highest rotation number tested.

When the protrusion surface is on the trailing side during CW rotation, one of the main differences when compared to dimples on the trailing side during CCW rotation is the fact that the heat transfer augmentation does not react as strongly to rotation. At low rotation numbers $Ro_b < -0.2$, the augmentation ratio increases slightly from 3.0 to 3.25 and 3.4 to 3.67 for $\delta = 0.2$ and 0.3, respectively. On further increase in rotation number, the heat transfer augmentation increases slightly or remains nearly constant. This is in contrast to when dimples are placed on the trailing surface resulting in a large increase in the augmentation ratio with rotation. However, protrusions on the leading side during CCW rotation behave similar to dimples and experience a large decrease in heat transfer. At low rotation numbers $Ro_b < 0.2$, there is a sharp drop in augmentation ratio from the stationary value of 3.0 to

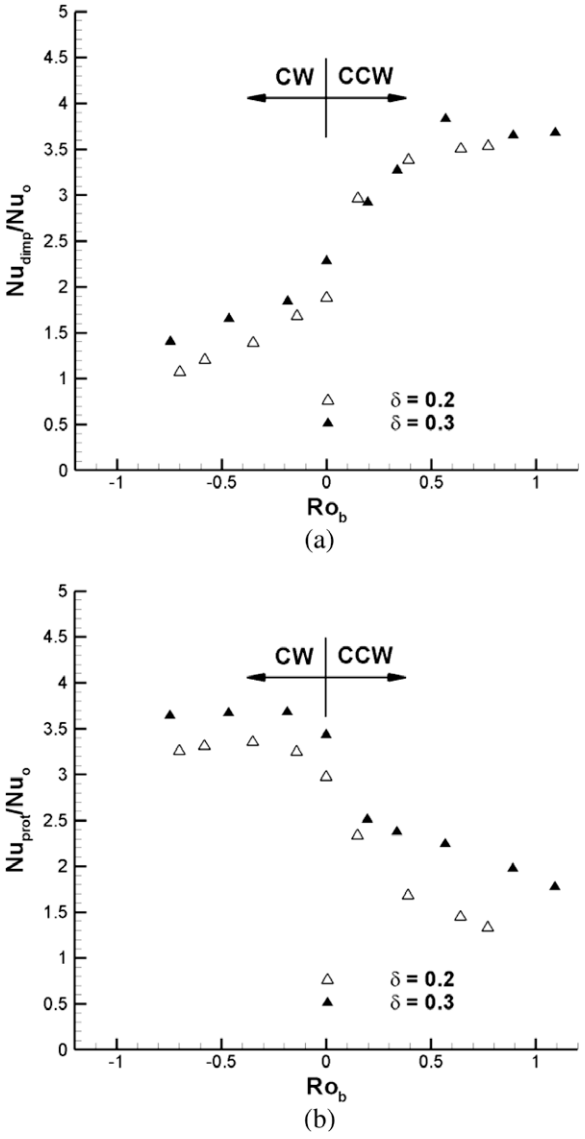

Fig. 17. Time averaged area weighted Nusselt number of the: (a) dimple side; (b) protrusion side for both dimple depths.

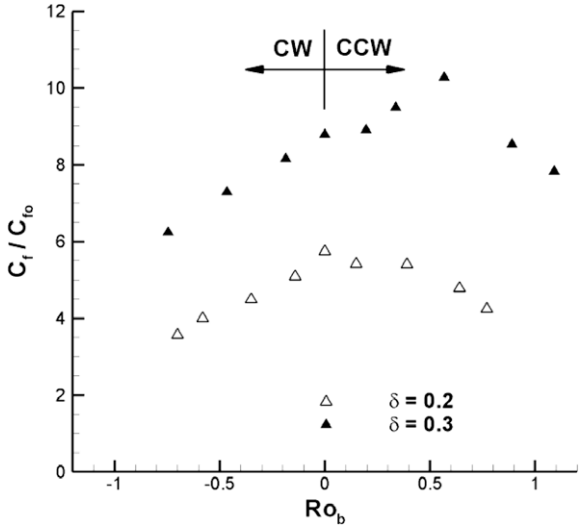

Fig. 18. Friction coefficient ratio of the rotating channel with dimples/protrusions for $\delta = 0.2$ and 0.3.

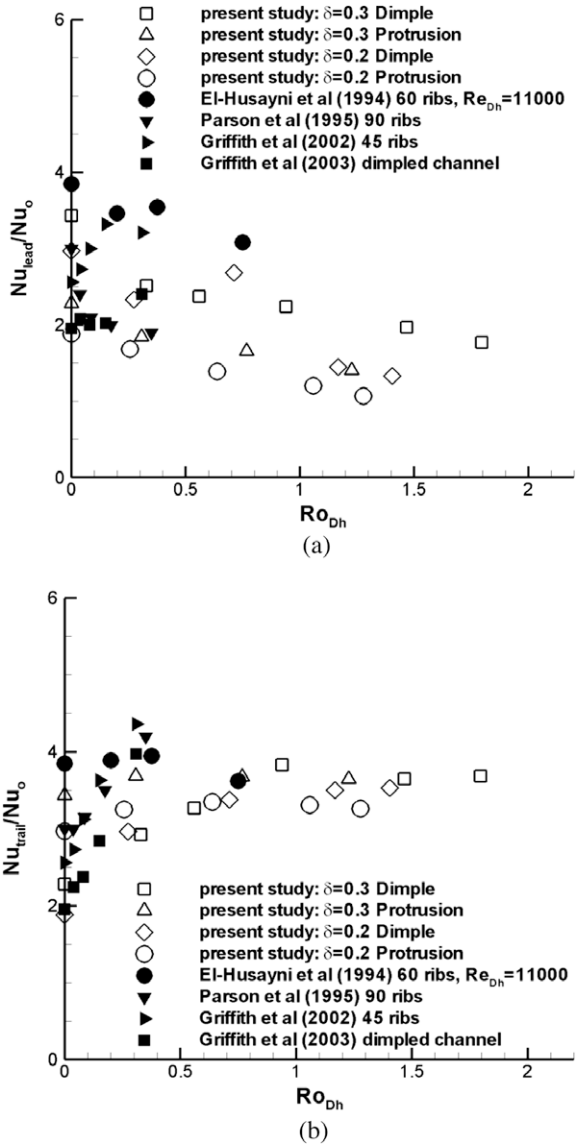

Fig. 19. Comparison of Nusselt augmentation levels of the present study with experimental results for: (a) leading surface; (b) trailing surface.

2.3 for $\delta = 0.2$, and from 3.43 to 2.43 for $\delta = 0.3$. The initial sharp drop is followed by a more gradual monotonic decrease to 1.3 at $Ro_b = -0.77$ and to 1.8 at $Ro_b = 1.1$ for $\delta = 0.2$ and 0.3, respectively.

In summary, in the stationary channel, the augmentation ratio is higher on the protrusion side than the dimple side of the channel. During CCW rotation, the dimpled surface on the trailing side experiences a large increase in heat transfer coefficient whereas the protrusion surface on the leading side experiences a large drop in augmentation. During CW rotation, while the dimpled leading side experiences a large drop in heat transfer, the trailing protrusion side does not benefit much from rotation.

Fig. 18 shows the friction ratio for the two dimple–protrusion depths over the full range of rotation numbers. Friction ratios range from 8.5 to 10 when dimples are placed on the trailing side versus 6.2–8.5 when protrusions are placed on the trailing side for $\delta = 0.3$. The increase in friction is much lower for $\delta = 0.2$, with values ranging from 3.5 to 5.7 and from 4.2 to 5.7, when protrusions or dimples are on the trailing side, respectively.

To put the current results in perspective, Fig. 19 shows a comparison of the heat augmentation levels of the dimple/protrusion

Table 5
Experimental heat transfer in rib and dimple roughened channels.

Experimental work	Surface condition	*Ro*	*Re*	$\Delta\rho/\rho$
El-Husayni et al. (1994)	Square channel with 60° staggered ribs	0–1.78	5000–23,000	
Parson et al. (1995)	Square channel with 90° ribs	0–0.35	2500–25,000	0.07, 0.1
Griffith et al. (2002)	Rectangular channel (AR = 4) with 45° ribs	0–0.3	5000–40,000	0.122
Griffith et al. (2003)	Rectangular channel (AR = 4) with dimples	0–0.3	5000–40,000	0.122

geometry with the experimental results of El-Husayni et al. (1994) for 60° staggered ribs, Parson et al. (1995) for 90° ribs, Griffith et al. (2002) for 45° ribs, and Griffith et al. (2003) for dimpled channel plotted against the rotation numbers based on the hydraulic diameter (D_h). These comparisons are not under similar conditions, Table 5, but nevertheless give a reasonable assessment of the dimple–protrusion geometry with respect to some of its peers in the literature. Heat augmentation levels on the leading surface, Fig. 19a, are lower than those of the skewed ribs (45° and 60°) but are comparable to those of normal ribs and dimpled channel, especially with the dimple on the leading side. On the other hand, the heat augmentation levels on the trailing side, Fig. 19b, are comparable to those of ribbed channels, especially for the deeper dimple depth ($\delta = 0.3$). While no friction data is provided in the experimental studies, overall it can be concluded that surfaces with dimple/protrusion roughness result in performance comparable to ribbed channels at a lower pressure drop penalty.

7. Summary and conclusions

Large-eddy simulations are used to investigate the effect of Coriolis forces and dimple depth on heat transfer and friction in a channel with dimples and protrusions on either side. Two geometries with two different dimple depths, $\delta = 0.2$ and 0.3 are investigated for a wide range of rotation numbers, $Ro_b = -0.77$ to 1.10. During negative or clockwise (CW) rotation, protrusions are on the trailing side of the channel, whereas during positive or counter-clockwise (CCW) rotation, dimples are on the trailing side of the duct.

Rotational Coriolis forces have the following effects on the mean flow and turbulence:

- CCW rotation energizes the flow on the trailing dimple wall and induces early reattachment in the dimple cavity increasing the strength of the flow ejection out of the dimple cavity. On the protrusion side, the less energetic flow results in a gradual growth of the wake region as the rotation number increases. In addition, a secondary flow consisting of two counter-rotating flow structures appears in the cross-section, one over the dimple and the other above the flat landing downstream of the dimple. The secondary flow strengthens as the rotation number increases and plays an important role in transporting cross-stream momentum from the trailing to the leading side. CCW rotation increases the volume-averaged TKE values in the domain up to a rotation number of approximately 0.5–0.6, after which it decreases.
- The effect of CW rotation on the trailing protrusion surface is not very strong. There is some effect on the protrusion wake which shrinks in size initially but which does not change significantly as rotation increases further. On the leading dimpled surface, the less energetic flow results in delayed reattachment of the separated shear layer with the recirculation zone extending across the whole dimple. No distinct secondary flow structures could be identified in this case and unlike CCW rotation, the volume-averaged TKE decreases with rotation number.

The effects on heat transfer are summarized as follows:

During CCW rotation, the dimpled surface on the trailing side experiences a large increase in heat transfer coefficient from an augmentation ratio of 1.9 for stationary flow to 3.5 at $Ro_b = 0.77$ for $\delta = 0.2$, and from 2.3 to a maximum of 3.8 for $\delta = 0.3$. The protrusion surface on the leading side also experiences a large drop in augmentation from 3.0 for a stationary channel to 1.3 at $Ro_b = 0.77$ for $\delta = 0.2$ and from 3.4 to 1.8 at $Ro_b = 1.1$ for $\delta = 0.3$. During CW rotation, the dimpled leading side experiences a large drop in heat transfer to between augmentation ratios of 1.1 and 1.4 for the two dimple depths, the trailing protrusion side does not benefit much from rotation – only increasing the augmentation ratio to between 3.25 and 3.7 from the stationary values of 3.0 and 3.4 for $\delta = 0.2$ and 0.3, respectively. These results lead to the conclusion that for low rotation numbers $|Ro_b| < 0.2$, placing protrusions on the trailing side is advantageous, whereas for $Ro_b > 0.2$, dimples on the trailing side of the duct will give better overall performance. Between the two dimple depths, the deeper dimple gives higher heat transfer augmentation at the price of more frictional losses ranging from 6 to 10 for $\delta = 0.3$ versus 3 to 5 for $\delta = 0.2$.

Acknowledgments

The calculations were performed on Virginia Tech's Terascale computing facility, System-X. The allocation grant and support provided by the staff is gratefully acknowledged.

References

Abdel-Wahab, S., Tafti, D.K., 2004. Large eddy simulations of flow and heat transfer in a 90 ribbed duct with rotation – effect of Coriolis and centrifugal buoyancy forces. J. Turbomach. 126 (4), 627–636.
Afanasyev, N.V., Chudnovsky, Ya P., Leontiev, A.I., Roganov, P.S., 1993. Turbulent flow friction and heat transfer characteristics for spherical cavities on a flat plate. Exp. Thermal Fluid Sci. 7, 1–8.
Al-Hadhrami, L., Han, J.C., 2003. Effect of rotation on heat transfer in two-pass square channels with five different orientations of 45° angled rib turbulators. Int. J. Heat Mass Transfer 46, 653–669.
Cui, J., Tafti, D.K., 2002. Computations of flow and heat transfer in a three-dimensional multilouvered fin geometry. Int. J. Heat Mass Transfer 45, 5007–5023.
Dutta, S., Han, J.C., 1996. Local heat transfer in rotating smooth and ribbed two-pass square channels with three channel orientations. J. Heat Transfer 118, 578–584.
El-Husayni, H.A., Taslim, M.E., Kercher, D.M., 1994. Experimental heat transfer investigation of stationary and orthogonally rotating asymmetric and symmetric heated and turbulated channels. J. Turbomach. 116, 124–132.
Elyyan, M.A., Rozati, A., Tafti, D.K., 2008. Investigation of dimpled fins for heat transfer enhancement in compact heat exchangers. Int. J. Heat Mass Transfer 51, 2950–2966.
Elyyan, M.A., Tafti, D.K., 2008. Effect of Coriolis forces in a rotating channel with dimples and protrusions. In: Proceedings of ASME-IMECE2008, Paper No. IMECE2008-66677.
Fann, S., Yang, W.J., Zhang, N., 1994. Local heat transfer in a rotating serpentine passage with rib-roughened surfaces. Int. J. Heat Mass Transfer 37 (2), 217–228.
Germano, M., Piomelli, U., Moin, P., Cabot, W.H., 1991. A dynamic subgrid-scale eddy viscosity model. Phys. Fluids 3, 1760–1765.
Griffith, T.S., Al-Hadhrami, L., Han, J.C., 2002. Heat transfer in rotating rectangular channels (AR = 4) with angled ribs. J. Turbomach. 124, 617–625.
Griffith, T.S., Al-Hadrami, L., Han, J.C., 2003. Heat transfer in rotating rectangular cooling channels (AR = 4) with dimples. J. Turbomach. 125 (3), 555–563.
Hseih, S.S., Chin, H.J., 2003. Turbulent flow in a rotating two pass ribbed rectangular channel. J. Turbomach. 125, 609–622.
Incropera, F.P., DeWitt, D.P., 2002. Fundamentals of heat and mass transfer, fifth ed. John Wiley, NY.

Johnson, B.V., Wagner, J.H., Steuber, G.D., Yeh, F.C., 1994. Heat transfer in rotating serpentine passages with trips skewed to the flow. J. Turbomach. 116, 113–123.

Ligrani, P.M., Harrison, J.L., Mahmood, G.I., Hill, M.L., 2001a. Flow structure due to dimple depressions on a channel surface. Phys. Fluids 13 (11), 3442–3451.

Ligrani, P.M., Mahmood, G.I., Harrison, J.L., Clayton, C.M., Nelson, D.L., 2001b. Flow structure and local Nusselt number variation in a channel with dimples and protrusions on opposite walls. Int. J. Heat Mass Transfer 44, 4413–4425.

Ligrani, P.M., Oliveira, M.M., Blaskovich, T., 2003. Comparison of heat transfer augmentation techniques. AIAA J. 41 (3), 337–362.

Lilly, D.K., 1992. A proposed modification of the Germano subgrid-scale eddy viscosity model. Phys. Fluids A 4 (3), 633–635.

Mahmood, G.I., Ligrani, P.M., 2002. Heat transfer in a dimpled channel: combined influences of aspect ratio, temperature ratio, Reynolds number, and flow structure. Int. J. Heat Mass Transfer 45, 2011–2020.

Mahmood, G.I., Sabbagh, M.Z., Ligrani, P.M., 2001. Heat transfer in a channel with dimples and protrusions on opposite walls. J. Thermophys. Heat Transfer 15 (3), 275–283.

Moin, P., Squires, K., Cabot, W., Lee, S., 1991. A dynamic sub-grid-scale model for compressible turbulence and scalar transport. Phys. Fluids A 3 (11), 2746–2757.

Moon, H.K., O'Connel, T., Glezer, B., 2000. Channel height effect on heat transfer and friction in a dimpled passage. J. Turbomach. 122, 307–313.

Murata, A., Mochizuki, S., 1999. Effect of cross-sectional aspect ratio on turbulent heat transfer in an orthogonally rotating rectangular smooth duct. Int. J. Heat Mass Transfer 42, 3803–3814.

Najjar, F.M., Tafti, D.K., 1996. Study of discrete test filters and finite difference approximations for the dynamic subgrid-scale stress models. Phys. Fluids 8, 1076–1088.

Parson, J.A., Han, J.C., Zhang, Y.M., 1995. Effects of model orientation and wall heating condition on local heat transfer in a rotating two-pass square channel with rib turbulators. Int. J. Heat Mass Transfer 38 (7), 1151–1159.

Patankar, S.V., Liu, C.H., Sparrow, E.M., 1977. Fully developed flow and heat transfer in ducts having streamwise-periodic variations of cross-sectional area. J. Heat Transfer 99, 180–186.

Sewall, E.A., 2005. Large eddy simulations of flow and heat transfer in the developing and 180 bend regions of ribbed gas turbine blade internal cooling ducts with rotation-effect of Coriolis and centrifugal buoyancy forces. PhD Dissertation, Virginia Tech.

Sewall, E.A., Tafti, D.K., 2008. Large Eddy simulation of flow and heat transfer in the developing flow region of a rotating gas turbine blade internal cooling duct with coriolis and buoyancy forces. J. Turbomach. 130 (1), 011005.

Sewall, E.A., Tafti, D.K., Graham, A.B., Thole, K.A., 2006. Experimental validation of large eddy simulations of flow and heat transfer in a stationary ribbed duct. Int. J. Heat Fluid Flow 27 (2), 243–258.

Tafti, D.K., 2001. GenIDLEST – A scalable parallel computational tool for simulating complex turbulent flows. In: Proceedings of the ASME Fluids Engineering Division, FED, vol. 256.

Viswanathan, A.K., Tafti, D.K., 2005. Detached eddy simulation of turbulent flow and heat transfer in ribbed duct. J. Fluids Eng. 127, 888–896.

Wagner, J.H., Johnson, B.V., Hajek, T.J., 1991a. Heat transfer in rotating passages with smooth walls and radial outward flow. J. Turbomach. 113, 42–51.

Wagner, J.H., Johnson, B.V., Kopper, F.C., 1991b. Heat transfer in rotating serpentine passages with smooth walls. J. Turbomach. 113, 321–330.

Won, S.Y., Zhang, Q., Ligrani, P.M., 2005. Comparisons of flow structure above dimpled surfaces with different dimple depths in a channel. Phys. Fluids 17 (4), 045105.